UC Irvine
UC Irvine Previously Published Works

Title

Observation of Preferential Pathways for Oxygen Removal through Porous Transport Layers of Polymer Electrolyte Water Electrolyzers

Permalink

https://escholarship.org/uc/item/86c8328m

Journal

iScience, 23(12)

ISSN

2589-0042

Authors

Satjaritanun, Pongsarun
O'Brien, Maeve
Kulkarni, Devashish
et al.

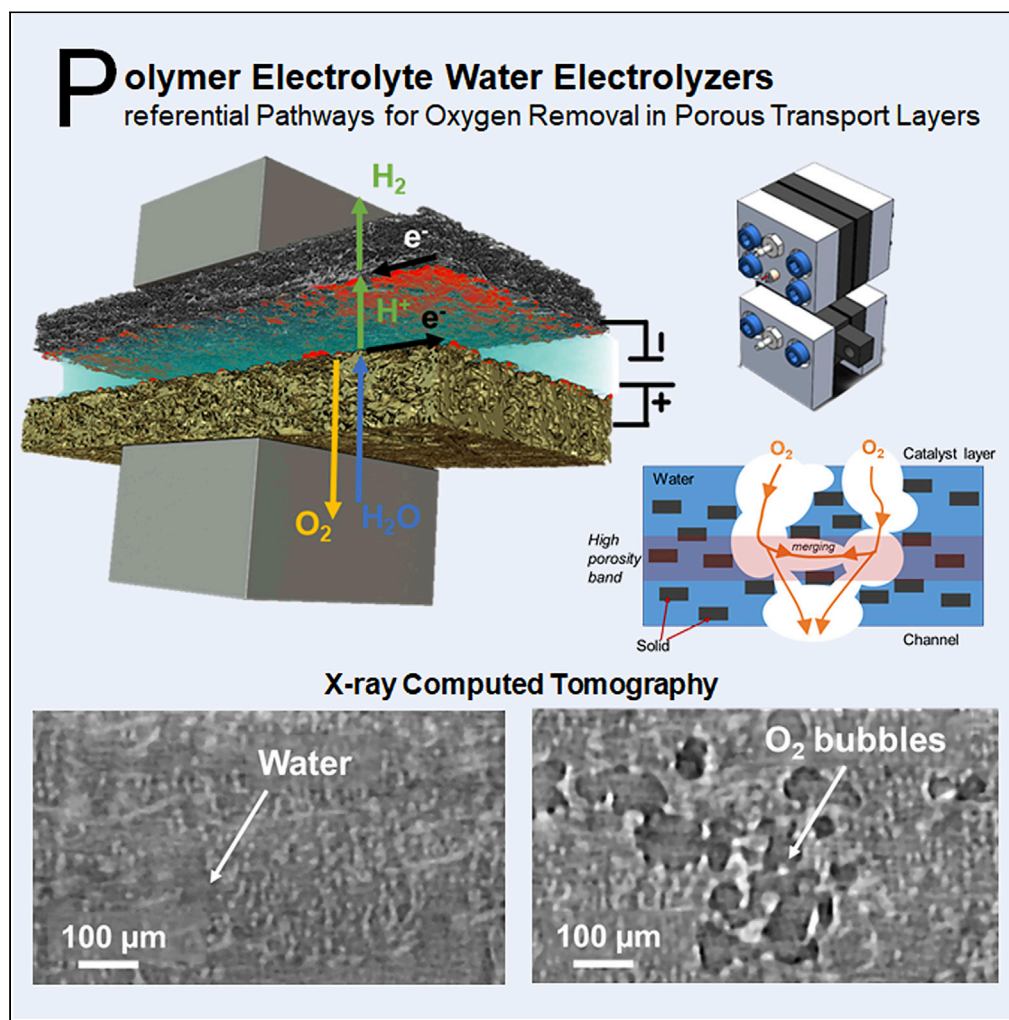**Publication Date**

2020-12-01

DOI

10.1016/j.isci.2020.101783

Peer reviewed

Article

Observation of Preferential Pathways for Oxygen Removal through Porous Transport Layers of Polymer Electrolyte Water Electrolyzers

Pongsarun Satjaritanun, Maeve O'Brien, Devashish Kulkarni, ..., Nemanja Danilovic, Dilworth Y. Parkinson, Iryna V. Zenyuk

iryna.zenyuk@uci.edu

HIGHLIGHTS

O_2 pathways in the PTLs of a water electrolyzer were observed with operando X-ray CT

Periodicity of the O_2 transport pathway observed here with the period of 400 μm

O_2 is taking preferential pathways through PTLs at various water flow rates and currents

Merging of oxygen front in the middle of PTL is observed due to good in-plane transport

iScience

Article

Observation of Preferential Pathways for Oxygen Removal through Porous Transport Layers of Polymer Electrolyte Water Electrolyzers

Pongsarun Satjaritanun,[1,6] Maeve O'Brien,[2,6] Devashish Kulkarni,[2] Sirivatch Shimpalee,[3] Cristopher Capuano,[4] Katherine E. Ayers,[4] Nemanja Danilovic,[5] Dilworth Y. Parkinson,[5] and Iryna V. Zenyuk[1,2,7,*]

SUMMARY

Understanding the relationships between porous transport layer (PTL) morphology and oxygen removal is essential to improve the polymer electrolyte water electrolyzer (PEWE) performance. *Operando* **X-ray computed tomography and machine learning were performed on a model electrolyzer at different water flow rates and current densities to determine how these operating conditions alter oxygen transport in the PTLs. We report a direct observation of oxygen taking preferential pathways through the PTL, regardless of the water flow rate or current density (1-4 A/cm^2). Oxygen distribution in the PTL had a periodic behavior with period of 400 μm. A computational fluid dynamics model was used to predict oxygen distribution in the PTL showing periodic oxygen front. Observed oxygen distribution is due to low in-plane PTL tortuosity and high porosity enabling merging of oxygen bubbles in the middle of the PTL and also due to aerophobicity of the layer.**

INTRODUCTION

The polymer electrolyte water electrolyzer (PEWE) is an essential part of a renewable energy economy. It uses renewable electricity to convert water into oxygen and hydrogen (Carmo et al., 2013). The product of interest from water electrolysis is hydrogen, a fuel that can be easily stored as compressed gas, transported via natural gas pipelines, and then combusted as a fuel or converted back to electricity in polymer electrolyte membrane (PEM) fuel cells. The produced hydrogen gas has a specific energy density of 120 MJ/kg, whereas gasoline has a specific energy density of 44 MJ/kg; this difference in specific energy density values is what makes hydrogen an attractive alternative fuel, as hydrogen has approximately 2.7 times the amount of energy per kilogram than liquid gasoline (Mazloomi and Gomes, 2012). Although water electrolysis is a well-established method for producing hydrogen, there remain several knowledge gaps to maximize efficiency in converting water to hydrogen and oxygen while minimizing production cost (Babic et al., 2017).

The overall electrochemical water splitting is divided into two half-cell reactions. When a potential is applied across a PEWE, an oxygen evolution reaction (OER) occurs on the anode and a hydrogen evolution reaction (HER) occurs on the cathode of the electrolyzer (Wang et al., 2019). For the OER, water flows in via the anode and transports through the porous transport layer (PTL) to reach the catalyst layer (CL). Once in contact with the electrocatalyst, two moles of water are split into four protons, four electrons, and one mole of oxygen gas. Byproduct oxygen exists the PEWE either as dissolved oxygen or in a gas phase. Residual oxygen bubbles can prove to be problematic during the operation of an electrolyzer, as it can block water from reacting with the electrocatalyst, thus decreasing the overall electrolyzer efficiency. Figure 1 shows a schematic of transport processes within a PEWE. Particularly, at high current densities, the mass transport losses are mainly caused by inefficient removal of oxygen from the electrolyzer (Suermann et al., 2015). In order to enhance the mass transport, the mechanisms of oxygen transport in the PTL need to fully be understood.

As an effort to better understand the two-phase transport behavior in the PTL, studies (Abdin et al., 2015; Dedigama et al., 2014; García-Valverde et al., 2012; Han et al., 2016; Kadyk et al., 2016; Kang et al., 2018; 2017; Kim et al., 2020; Lee et al., 2020a; Lee et al., 2017; Leonard et al., 2020; 2018; Lopata et al., 2020; Schuler et al., 2019; Seweryn et al., 2016; Suermann et al., 2017; Zlobinski et al., 2020) have focused on using

[1]Department of Chemical and Biomolecular Engineering, National Fuel Cell Research Center, University of California Irvine, Irvine, CA, USA

[2]Department of Material Science and Engineering, University of California Irvine, Irvine, CA, USA

[3]Department of Chemical Engineering, University of South Carolina, Columbia, SC, USA

[4]Nel Hydrogen, Wallingford, CT, USA

[5]Lawrence Berkeley National Laboratory, Berkeley, CA, USA

[6]These authors contributed equally

[7]Lead Contact

*Correspondence: iryna.zenyuk@uci.edu
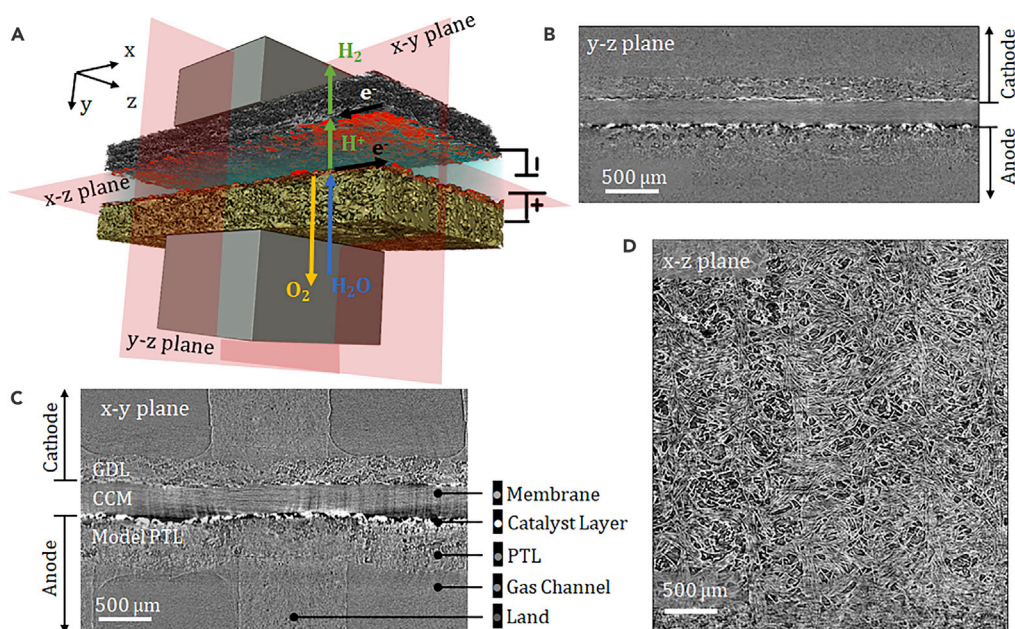
https://doi.org/10.1016/j.isci. 2020.101783

Figure 1. 3D Volume Rendering and the Cross-Sectional Tomographs for the PEWE Configuration
(A) 3D representation of a conventional PEWE obtained with X-ray CT, where the relevant viewing planes are highlighted, as well as transport processes are shown. The treated Freudenberg GDL is on the bottom, and the carbon paper Freudenberg GDL is on the top.
(B) Labeled cross section of the y-z plane and detailing of electrolyzer components.
(C) Labeled cross-sections of the x-y plane.
(D) Labeled cross-sections of the x-z plane, where the Weka training was done on this plane.

imaging techniques to investigate the evolution and transport of oxygen in electrolyzers, including optical, neutron, or X-ray imaging, as well as computational studies. Optical microscopy was utilized by Dedigama et al. (Dedigama et al., 2014) in order to study two-phase flow in an operating electrolyzer. With a 7,000 fps camera, as well as a transparent sheet and specific backlighting, they were able to capture anodic two-phase behavior with high temporal accuracy. Following this study, Lee et al. (Lee et al., 2017) employed a microfluidic platform, termed PTL-on-Chip, to study the effect of microstructure on the growth of oxygen bubbles, using an optical microscope. It was concluded that the morphology of the PTL has a significant impact on the governing force of the oxygen gas cluster growth and dictates the flow regime during PEWE operation.

Neutron radiography has been utilized by Seweryn et al. (Seweryn et al., 2016) to visualize steady-state oxygen distribution in the PTLs. They were able to observe oxygen residence time in a PTL, specifically porous titanium (Ti), and show an equilibrium in the two-phase flow in the PTL. Their observations surprising at a time, suggested that the PTL would always be saturated with water, regardless of the current density, and that oxygen saturation did not change with current density in the regime of 0.1–2.5 A/cm^2. Lee et al. (Lee et al., 2020a) have investigated the dynamic gas transport behavior in the anode PTL by using *operando* synchrotron X-ray imaging. When they applied the current with a steep ramp-up and a shallow ramp-down, they concluded that the oxygen responds more rapidly, which means that the gas saturation in the PTL reached a steady state quickly. Zlobinski et al. (Zlobinski et al., 2020) have studied the effect of the two-phase flow behavior within the PTLs under steady state and dynamic load of the electrolyzer by using a neutron imaging with high spatial resolution (6 μm) and relatively high temporal resolution (1 s exposure time). They concluded that the two-phase flow in the PTLs is purely capillary driven for a wide range of operating conditions and that viscous forces are negligible. They further confirmed the findings of Seweryn et al. that water and gas distribution is not affected by current density (from 10 to 2000 mA/cm^2). Leonard et al. (Leonard et al, 2018) were able to observe oxygen bubble formation and transport with X-ray computed tomography (CT) and radiography using *operando* hardware. This work demonstrated that as the current density increased, the residence time of oxygen bubbles in the channel decreased; this was expected, as higher current density would result in more oxygen being formed,

enabling faster oxygen bubbles detachment. With Ti PTLs currently, it is experimentally not possible to differentiate between water and oxygen in the PTL, as Ti is highly X-ray attenuating material. Therefore, limited information is known on microscale distribution of oxygen in the PTL and how PTL morphology can be tailored to remove oxygen more effectively, as the in-plane vs through-plane transport properties can be rationally designed.

The aim of this work is to investigate oxygen content in the PTLs and its relation to both PEWE current density and water flow rate, as well as understand whether oxygen takes preferential pathways when transporting through the PTL. So, a PEWE was set up with model carbon fiber PTLs (with similar morphological properties to Ti PTL) in order to directly observe and quantify both the oxygen content and preferential pathways oxygen could take as it exits PTL using *operando* X-ray CT. Using carbon fiber PTLs and short experimental imaging time enables direct observation of the steady-state pathways for oxygen transport within the carbon PTL. This is unprecedented, as no previous study has seen the pore-scale observation of oxygen content within the PTL with *operando* techniques. In order to distinguish oxygen within the PTL, machine learning was utilized to analyze the amount of oxygen present in the PTL of the electrolyzers at varying flow rates and current densities. The direct three-dimensional model-based lattice Boltzmann method (LBM) was used to better understand the physics behind the two-phase transport in the PTL under different cell operating conditions.

Experimental

X-Ray Computed Tomography (CT)

X-ray CT was conducted at the Advanced Light Source, on beamline 8.3.2, at the Lawrence Berkeley National Laboratory. The optics used were as follows: 50 μm LuAg:Ce scintillator, 5x lenses, a sCMOS PCO Edge camera, and a double multilayer monochromator. The X-ray energy selected was 26 keV. The resulting images had a voxel resolution of 1.3 μm and a horizontal field of view of 3.3 mm. The X-ray CT images required sample rotation (180 degrees), and therefore, special care had to be taken so that the water inlet and gas outlets, as well as the thermocouples, did not become tangled. These parameters resulted in a scan time of ∼6 min.

Materials

The catalyst-coated membranes (CCMs) used in this experiment were provided by NEL Hydrogen, Wallingford, CT, and consisted of CCMs with catalyst loadings of 3 mg/cm^2 of platinum (Pt) on the cathode and 3 mg/cm^2 of iridium oxide (IrOx) on the anode. Nafion 117 was used as a PEM. The PTLs were treated and untreated Freudenberg carbon papers (Fuel Cell Store, College Station, TX) without a microporous layer (MPL), for anode and cathode, respectively. Treatment was done in a piranha solution for five hours to make the PTL surface hydrophilic. The piranha solution treatment resulted in irreversible wettability modification, where the contact angle of the PTL was reduced from 133 ± 4° to about 0°. The PTLs completely took in water, indicating the completely hydrophilic surfaces. Furthermore, the PTL hydrophilicity was also confirmed with X-ray imaging as will be discussed later. Two Freudenberg gas diffusion layers (GDLs) with 50 % compression on the anode side were used to simulate morphology of the Ti PTLs. The compressed GDLs should have pore sizes of less than 10 μm in diameter, which is what the typical pore sizes for sintered Ti PTLs. In this study, treated Freudenberg at this compression has pore sizes comparable to the conventional PTL, which has the average pore size about 10 μm in diameter, as reported in Supplementary Information (SI), Figures S1 and S2. The main morphological difference between the carbon fiber PTL used in this study and Ti-based PTL is the different through-plane vs. in-plane tortuosities. The PTL studied here has an in-plane tortuosity of 1.3 (Figure S1D), whereas Ti PTL has in-plane tortuosity of 3.3–3.9 (Leonard et al., 2020). The cathode had untreated Freudenberg GDL. The anode and cathode bipolar plates (BPPs) were made of graphite, as operating time of electrolyzers was only several hours and therefore low corrosion currents were observed from using carbon PTL and carbon BPPs. Our earlier study proved that it is possible to operate a PEWE with carbon PTLs for short duration without significant carbon corrosion (Leonard et al., 2018). Furthermore, recent benchmarking study across leading PEWE laboratories in the world also used carbon layer instead of Ti for PTL to conduct the benchmarking round robin study (Bender et al., 2019).

RESULTS AND DISCUSSION

Interpreting Tomography Data

Figure 1 shows the 3D volume rendering and the cross-sectional tomographs for the PEWE configuration. The 3D volume rendering displays the composition and morphology of the PEWE, as shown in Figure 1A. At

the anode side, water was transported from the channel to the catalyst layer, and the oxygen product was removed from the catalyst layer. It is difficult to quantify oxygen content in the PTL by using only 3D visualization. The cross-sectional tomographs were created for ease of visualization and quantification. The relevant planes examined in this study are labeled and highlighted in Figure 1.

The y-z plane is used to understand how the oxygen content changed within the length of the PTL, as shown in Figure 1B. By area-averaging information in the y-z plane, oxygen content under land versus that under channel was found. It is used mostly to quantify land-channel effects on oxygen distribution. The x-y plane is the through-plane view where one can observe both channels, the land, the cathode GDL, the membrane, the catalyst layer, and the anode PTL in the same slice, as shown in Figure 1C. A tomograph "slice" is essentially a single reconstructed image that is used to build up the 3D data. This front-facing slice was used to determine the oxygen content along the length of the anode side PTL. The brightest spots near both sides of the PEM are the catalyst layers. This is due to the high X-ray attenuation of the catalyst materials (Ir and Pt) making them very distinguishable. At the x-z plane, oxygen appears as dark, as it has the lowest X-ray attenuation on the anode side, as shown in Figure 1D. Water and carbon have comparable X-ray attenuation, so it is difficult to render them separately; therefore, a single phase will be used to identify both in this study. The x-z plane, which is the in-plane or top-down view, was used to train the Weka machine learning algorithm in order to interpret the oxygen content throughout the PTL. In addition to using the x-z plane for interpreting the oxygen content in the PTL, it was also used with the z-project function in ImageJ to build an average of the amount of oxygen and the catalyst distribution.

The X-ray CT scan of an electrolyzer under open-circuit voltage (OCV) condition was performed to observe whether there is any residual oxygen trapped within the electrolyzer. Figure S5 compares a cross-sectional image of an identical location of an electrolyzer at the OCV and that at 1 A/cm^2, where all the PTL is filled with water. This image proves that piranha solution treatment of PTLs was successful and the PTL is mostly hydrophilic. From this figure, one can observe that the PTL under the land is more compressed than under the channel. This is to be expected, as the PTL was compressed by 50 % to achieve pore sizes comparable to those of Ti PTLs. The cathode PTL shows a lower degree of compression than cathode as expected given the target of 20 % compression on the cathode.

Oxygen Transport Pathways under Various Current Densities

Observing oxygen transport pathways is an important step toward understanding the transport of evolved oxygen and supplied water through the PTL. Figure 2 shows the x-y plane of the PEWE during cell operation at 1 A/cm^2 and 4 A/cm^2 with varied flow rates of water. The electrochemical data showing stable potentials at these current densities are shown in Figure S6 and overall polarization curves by Figure S7 at three water flow rates. The tomography cross sections were selected as representative of the whole domain and they reveal that the oxygen pathways are visible within the PTL. Figures 2A–2C present the x-y plane of a cell that operates at 1 A/cm^2 with the flow rates of 1 mlpm to 3 mlpm, respectively. False coloring on these cross sections provided an example of the oxygen transport pathways in the PTL. The result shows that oxygen content in the PTL did not change as water flow rate increased from 1 to 3 mlpm. There are several locations where oxygen goes all the way through from the catalyst layer to the channel or land. However, there are some locations showing that the oxygen is trapped in the PTL under the land area. Similar to the study by Leonard et al. (Leonard et al., 2020), there is more gas observed under the land areas. Comparing Figures 2A–2C at 1 A/cm^2 to Figure S5 at OCV, there is a significant amount of oxygen present in the PTL after the current density is applied compared to that at OCV, which will be quantified in the later sections.

Figures 2D–2F show the x-y cross-sectional tomographs of the PEWE that operates at 4 A/cm^2 with the flow rates of 1 mlpm to 3 mlpm, respectively. Comparing these operating conditions to 1 A/cm^2 at all flow rates, these figures appear virtually identical, although current densities are four times higher for Figures 2D-2F compared to Figures 2A–2C. Oxygen seems to follow the same pathways at 4 A/cm^2 as at 1 A/cm^2. No new pathways emerged for oxygen removal. The oxygen content for the PEWE operating at 2 A/cm^2 and 3 A/cm^2 is shown in Figure S8. Although these images are only 2D cross sections, the oxygen transport seems to follow the same pathways through the PTL, regardless of current density or water flow rate for the range studied.
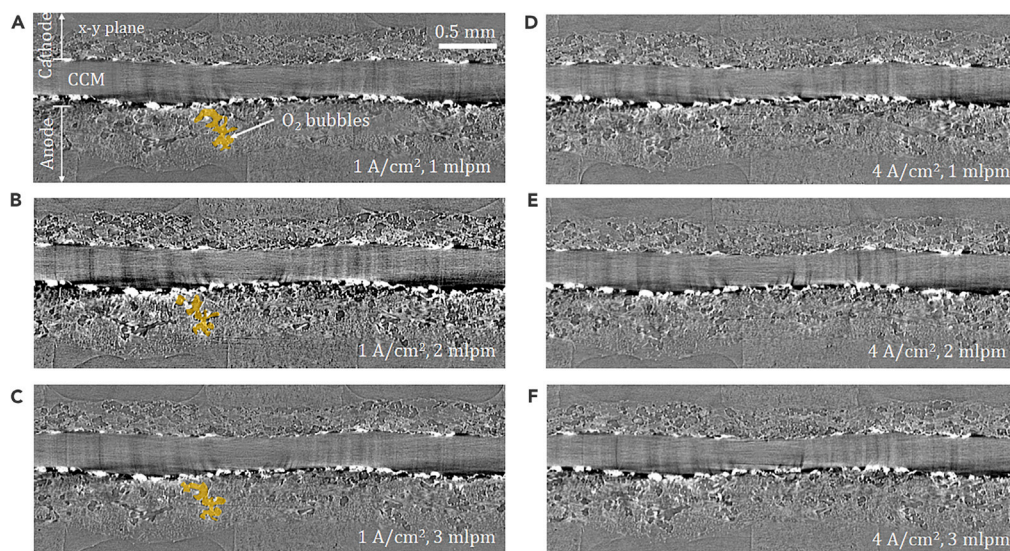
Figure 2. The x-y Cross-Sectional Tomographs of the PEWE during Cell Operation, and the Cell Temperature Was 60°C

(A) 1 A/cm^2, 1 mlpm.
(B) 1 A/cm^2, 2 mlpm.
(C) 1 A/cm^2, 3 mlpm.
(D) 4 A/cm^2, 1 mlpm.
(E) 4 A/cm^2, 2 mlpm.
(F) 4 A/cm^2, 3 mlpm.

Impact of Current Density and Flow Rate on Oxygen Transport in PTL

Oxygen bubbles may accumulate and become trapped in the pore space of the PTL, resulting in mass transport losses. Figure 3 shows averaged oxygen content within the PTL as a function of the PTL thickness. The PTL/catalyst layer interface is located at x = 0, whereas the flow field is located at x = 320 μm. The oxygen content in the channel is uncertain due to difficulty to quantify oxygen content within the interface of PTL and channel/land, showing no obvious trend among flow rates, yet this does not significantly impact the computed oxygen content in the PTL, especially near the catalyst layer. Figure 3A shows the comparison of oxygen content for 1 A/cm^2 at different flow rates. The oxygen content near the catalyst layer is between 30 and 40 %. Then, in the middle of the PTL, it decreases to about 15 %, and near the channel, it varies with flow rate. For the cell measurements at 1 A/cm^2, the cell was not fully conditioned, so more oxygen near the catalyst layer was observed, compared to operation at higher current densities. At 4 A/cm^2, oxygen content near the catalyst layer was 20–30 % and it decreased to 5 % near the flow field, after which it increased again when entering the channel, as shown in Figure 3B. The results for the other cell operating conditions were reported in Figure S9. From the overall measurement of oxygen content as a function of PTL thickness, the results show that there is a high oxygen content at the catalyst layer interface with the PTL. Gas transport pathways merge approaching the middle of the PTL. As mentioned above, some of the oxygen is trapped in the PTL near the land area but due to low in-plane tortuosity (shown by SI, Figure S1); for this type of PTL, the majority of oxygen is laterally removed from under the land into the channel.

Figure 3C shows the oxygen content comparison with varied currents at the same flow rate of 2 mlpm. Again, there seems to be no correlation between current density and oxygen content within the PTL. Zlobinski et al. (Zlobinski et al., 2020) and Seweryn et al. (Seweryn et al., 2016) were able to quantify water saturation in the PTL via neutron radiography. Zlobinski et al. confirmed the earlier Seweryn et al. study that oxygen content in PTLs did not change with current density from 0.1 to 2 A/cm^2. They showed that near the catalyst layer, the water and oxygen saturations were 0.5. In this study, oxygen content which is equivalent to oxygen saturation is approximately 0.2–0.4 near the catalyst layer. Oxygen content near the flow field is close to 0, in agreement with Zlobinski et al. Note that their PTL thickness is 1 mm, about 3 times higher than that used in our study, which increases the transport path length and leads to more oxygen accumulation near the catalyst layer. In the study by Lee et al., a 250-μm PTL was used in neutron
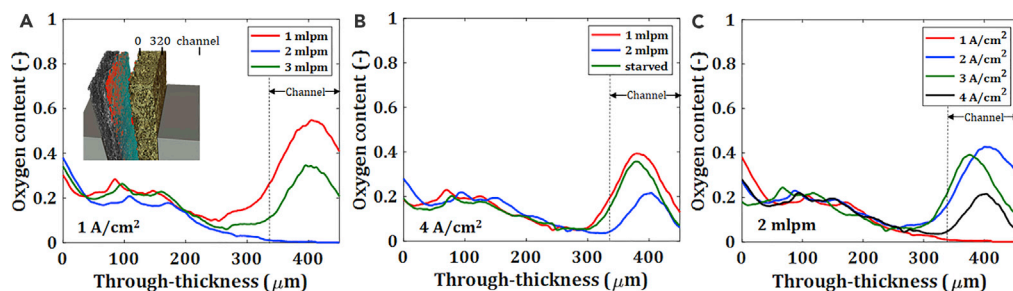
Figure 3. Oxygen Content as a Function of through-Thickness PTL Location
(A) The comparison of oxygen content at 1 A/cm^2 with varied water flow rates.
(B) The comparison of oxygen content at 4 A/cm^2 with varied flow rates.
(C) The comparison of oxygen content for varied current densities.

radiography study (Lee et al., 2020b), and they observed ∼0.3 oxygen saturation near the catalyst layer, which is close to the value obtained in this study.

Oxygen Transport Classification in Various Regions of the PTL

To better understand oxygen transport in the PTL, oxygen content within the three through-thickness portions of the PTL was investigated. Figure 4 shows the comparison of oxygen content distribution within the PTL at 1 A/cm^2 with the flow rate of 2 mlpm. The PTL was separated into three portions: near the catalyst layer interface (CL/PTL), middle of the PTL (mid PTL), and near the land/channel interface (PTL/channel), as shown at the top of Figure 4A. The through-plane view of oxygen content generated with the z-project (averaged from 3D volume and projected onto a single slice) is depicted in Figure 4A, where the volumetric information of oxygen content in the PTL was combined into a single image.

Figures 4C–4E show the in-plane view of oxygen content in the portions of catalyst layer/PTL, mid PTL, and PTL/channel, respectively. The location near the catalyst layer shows that the local oxygen content can be as high as 70 % in certain locations, mainly under the land; however, on average as shown in Figure 3, it is below 40 %. The oxygen content gradually decreases when transporting through the mid PTL and PTL/channel, respectively. The oxygen content of each portion was measured along the length of the sample and plotted, as shown in Figure 4B. The average oxygen content in each PTL portion from catalyst layer/PTL to PTL/channel was 35.7 %, 18.8 %, and 7.1 %, respectively. Thus, it roughly halved as oxygen transported through each of the 1/3 sections of the PTL. The results show that the distribution of oxygen content seems to be a "spatially periodic front", especially at the mid PTL and PTL/channel portions. The spatial pattern is parallel to the land channel location and is in the same direction of water flow. The oxygen peaks appear every 400 µm, where the oxygen peaks vary from 12 to 25 %, whereas the oxygen content valleys (water-rich locations) vary from 2.5 to 7 %.

Figure 5 presents the oxygen content comparison in the three portions of the PTL for the PEWE operating at 4 A/cm^2 with the water flow rate of 2 mlpm. The result shows that the average oxygen content in each PTL portion from CL/PTL to PTL/channel is 27.5 %, 18.4 %, and 7.5 %, respectively, as shown in Figure 5B. These values are slightly lower than the ones observed for operation at 1 A/cm^2. As explained before, at 1 A/cm^2, the CCM was most likely not fully conditioned well, not reaching its full steady state. Peaks in the oxygen content are observed below the land regions, similar to the case of 1 A/cm^2, indicating that some oxygen was trapped under the land. Figures S10 and S11 show oxygen content within three selected regions for the PEWE operating at 2 and 3 A/cm^2 and water flow rate of 2 mlpm, showing very similar distributions to Figures 4 and 5, confirming that the oxygen prefers the same transport pathways through the PTL, regardless of current density. And Figure S12 compares oxygen distributions across current densities and flow rates.

The spatially periodic oxygen front observed here for all the current densities has not been reported before. We provide several hypotheses to explain its physics, which we will attempt to prove or disprove: (1) oxygen periodic front is due to catalyst layer inhomogeneous distribution, (2) electrochemical decoupling of catalyst sites due to local oxygen flooding at the catalyst sites, (3) interplay between in-plane/ through-plane PTL morphology, wettability and resulting bubble coalescence and transport. Regarding
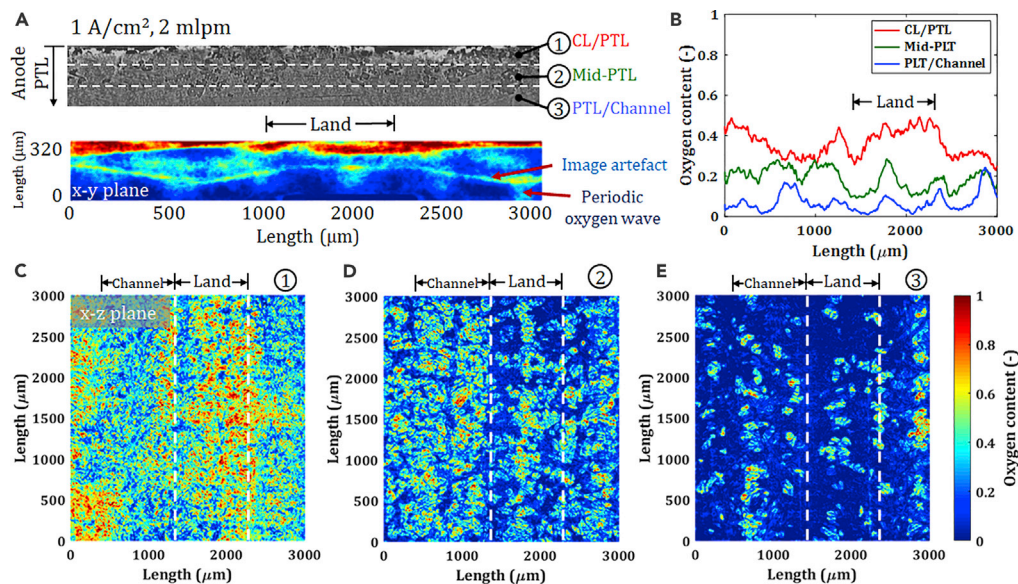
Figure 4. The Comparison of Oxygen Content within the Different Portions of the PTL at the Operating Condition of 1 A/cm², and 2 mlpm

(A) (Top) 1-3 portions of the PTL that located CL/PTL interface, middle of PTL, and PTL/channel interface. (Bottom) 2D oxygen content of the PTL at x-y plane by using the Z-project method.

(B) Oxygen content comparison within the different PTL portions as a function of distance.

(C) Z-project of the oxygen content of the x-z plane at the CL and PTL interface.

(D) Z-project of the oxygen content of the x-z plane in the middle PTL portion.

(E) Z-project of the oxygen content of the x-z plane at the PTL and channel interface.

hypothesis 1, we plotted catalyst layer distribution and correlated it to the oxygen waveform. Figure S13 shows a map of catalyst distribution. There was little to no correlation found between the catalyst distribution and the oxygen content, as correlation coefficients are below 0.1 (Figure S13C). Hypothesis 2 attempts to explain the periodicity in oxygen front with electrochemical decoupling of the catalyst sites. As when the oxygen locally saturates the catalyst layer, catalyst will not be active toward splitting water due to either proton limitations or unavailability of water vapor; however, after oxygen diffuses away, the catalyst becomes active again. In general, within the catalyst layer, the IrOx is hydrophilic and it is likely that liquid water is present either within the ionomer or directly on the surface of the catalyst; if that is not the case, water can react in the vapor phase, as well (Fornaciari et al., 2020). There are no literature studies investigating the length scale of these decoupling phenomena. In this study, the periodic oxygen front was found to be pronounced in the location of 160 μm, away from the catalyst layer, which is a half of the PTL thickness, as shown in Figures 4A and 5A. Therefore, this hypothesis is unlikely; however, we did perform additional model simulations with this options (see Figures S14 and S15 and discussion in SI). And these model simulations did not predict the experimentally observed oxygen wave front. Therefore, we believe it is transport and not kinetics that is responsible for the periodic oxygen front observation.

This periodicity is perhaps due to oxygen taking preferential pathways as it exits the PTL, which would account for the apparent periodicity, hypothesis 3. Zlobinski et al. (Zlobinski et al., 2020) suggest that the pore network inherent to a porous media – in their case it was sintered Ti PTL – could account for the gas traps. Gas traps are areas of either high hydrophobicity or hydrophilicity inherent to a porous media. Since the PTL was well treated and OCV data show no hydrophobic locations within the PTL, it is difficult to explain the periodicity with the gas traps. Instead, we believe that the observed oxygen removal is due to different PTL in-plane vs through-plane tortuosities, 1.3 vs. 1.7, its wettability (completely aerophobic), and pore-size distribution. We explore the third hypothesis in more detail in the next section using a multi-physic model.

Modeling of Oxygen Transport in the PTL

Figure 6 shows the comparison of oxygen content in the PTL between the computational fluid dynamics (CFD) simulation and the experimental data at 1 and 4 A/cm² having water flow rate of 2 mlpm. The
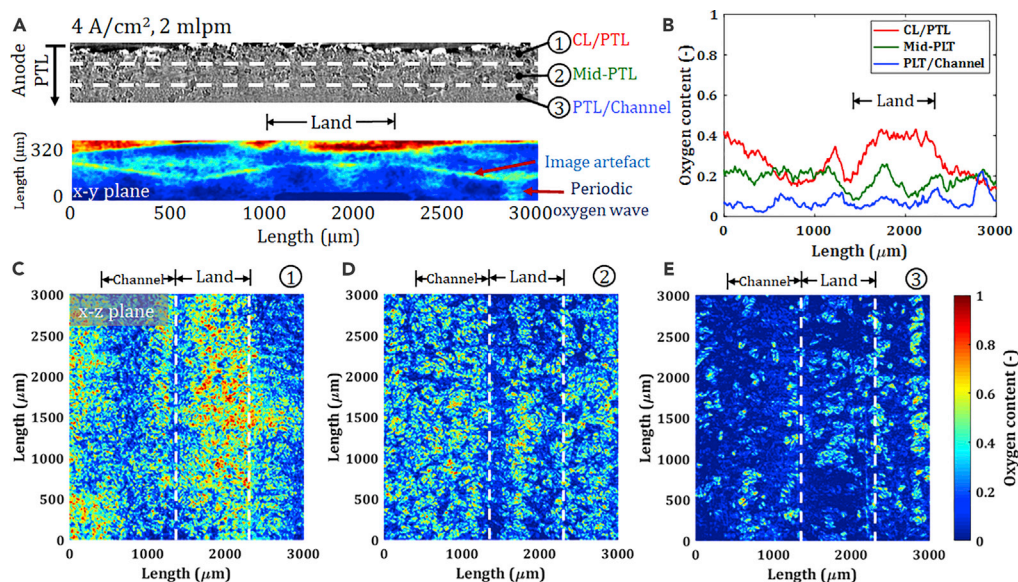
Figure 5. The Comparison of Oxygen Content within the Different Portions of the PTL at the Operating Condition of 4 A/cm², 2 mlpm

(A) (Top) 1-3 portions of the PTL that located CL/PTL interface, middle of PTL, and PTL/channel interface. (Bottom) 2D oxygen content of the PTL at x-y plane by using the Z-project method.

(B) Oxygen content comparison within different PTL portions as a function of distance.

(C) Z-project of the oxygen content of the x-z plane at the CL and PTL interface.

(D) Z-project of the oxygen content of the x-z plane in the middle PTL portion.

(E) Z-project of the oxygen content of the x-z plane at the PTL and channel interface.

CFD simulations were able to adequately predict oxygen content in the PTL having aerophobic pores (water contact angle of 10°), especially in the middle and at the interface with the flow field, as evidenced by the agreement of average oxygen content with experimental data (Figures 6C and 6D). The model overpredicts oxygen content near the catalyst layer by 10 %. Oxygen content in the PTL for 1 A/cm² and 4 A/cm² predicted by the model is very similar, and oxygen pathways do not change when current density is increased. The shape of the oxygen front is somewhat different, also periodic but with the period of 200 μm, which is half of that observed experimentally. Furthermore, the simulations reveal that more oxygen was trapped in the PTL under the land area, compared to the experimental observations.

To understand the differences between experimental and CFD data, we need to better understand model assumptions, physics incorporated, and its current limitations. These are listed in the SI, but we will focus on the most relevant assumptions here. Within the model, oxygen bubbles nucleate within the catalyst layer with the nucleation radius of 1 μm and nucleation site density of 1 site/μm. The exact location and density of the nucleation sites and bubble nucleation radius are not well known, although other studies have assumed 1 nm nucleation radius (Kadyk et al., 2016). Generally, oxygen is formed in dissolved form and nucleates over the hydrophobic defects, when the dissolved oxygen critical saturation concentration is reached. We cannot determine here from the experimental data whether oxygen bubble nucleation is uniform over the catalyst layer area due to the resolution limitation. Once the bubble nucleates, its radius will grow to a critical size and it will detach from the nucleation site and the next bubble will nucleate and grow and the process will repeat. The radius of a bubble upon detachment depends on mechanical balance of forces, such as buoyancy, pressure, capillary, drag, and lift. The shape and size of the bubble can be characterized by the Eotvos (Eo) number, which is correlated to gravity, g, density difference between fluids, $\Delta\rho$, and surface tension, σ:

$$Eo = \frac{\Delta\rho g b^2}{\sigma} \qquad \text{(Equation 1)}$$

where b is characteristic length scale taken to be the mean size of the pores of the PTL of 10.3 μm in this work. The calculated Eo number was 1.36×10^{-4}, and the parameters used for calculation are reported
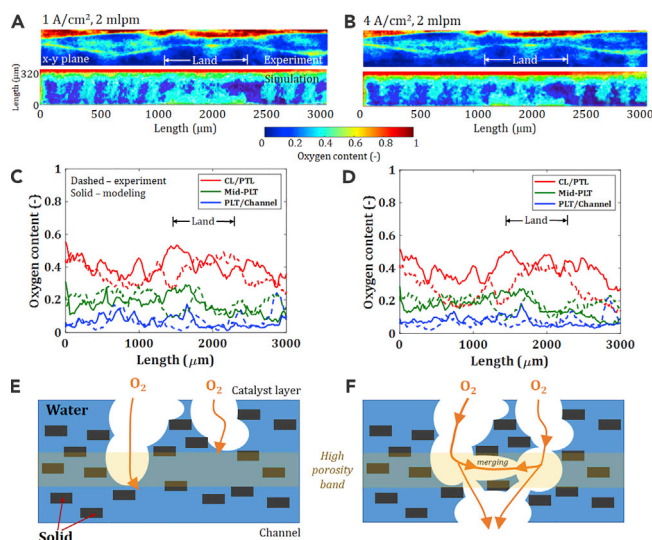
Figure 6. The Comparison of Oxygen Content in the PTL between the CFD Simulation and the Experimental Data at 1 and 4 A/cm^2 with Water Flow Rate of 2 mlpm

(A) CFD simulation comparison with experimental results at the operating condition of 1 A/cm^2, 2 mlpm.

(B) CFD simulation comparison with experimental results at the operating condition of 4 A/cm^2, 2 mlpm.

(C) Average oxygen content for the three domains selected comparing CFD and experiment results for 1 A/cm^2.

(D) Average oxygen content for the three domains selected comparing CFD and experiment results for 4 A/cm^2 current densities.

(E and F) A conceptual schematic showing transport of oxygen in the PTL.

in Table S1. Eo << 1 indicates that the bubble transport is dominated by the surface tension and hence capillary forces are dominant, whereas gravity and buoyancy are minor driving forces. (Sattari et al., 2020) From here, it is evident that bubble shape and path of transport will be determined by PTL wettability and pore size distribution, as well as current density (oxygen gas pressure). The pore size distribution of this PTL sample is shown in the SI Figure S1E.

The wettability of the PTL in this study is the following: it is hydrophilic and aerophobic. Oxygen first will displace water from the large hydrophilic pores and then from the small hydrophilic pores. If any hydrophobic pores are present, then oxygen will first fill those before advancing into the hydrophilic domains; however, here we do not observe hydrophobic pores. The shape of the oxygen bubbles will always be concave, as water has convex menisci in the hydrophilic porous media. Thus, the bubble transport will be guided by the pore size distribution of the PTL, as shown by Figures 6E and 6F. Oxygen will nucleate and grow as bubbles at the surface of the catalyst layer, transport through the large pores of the PTL displacing water. The PTL selected here has good in-plane transport properties and also large porosity in the middle of the PTL, as shown by Figure S2; therefore, oxygen gas will merge and coalesce in plane, as these are the pores of low resistance before finally transporting into the channel. The high-porosity band in the middle of the PTL is mainly due to two PTL layers stacked together in this study and it allows oxygen to merge and to form a periodic waveform. Note that the PTL does not have porosity that replicates oxygen pattern here. Once the pathway is established for oxygen removal, the energy it takes for oxygen to form a new pathway is much higher than that for it to take the established pathway. The flux of oxygen will be higher at higher current densities, but the oxygen pathways remain the same. Therefore, the morphology of the PTL determines the expulsion pathways through which oxygen travels. As discussed above, the model physics do not currently capture the nucleation and growth of bubbles at the catalyst layer surface effectively, and we believe this causes the deviation between the modeling and experimental results. This study is also performed with a CFD simulation with a uniform flux of oxygen and a PTL that is aerophilic (water contact angle of 170°), as shown in Figures S16 and S17. The simulations show that the oxygen transport pathways did not change from 1 to 4 A/cm^2 and no periodicity in oxygen removal was observed. Additionally, we explored the PTL contact angle of 10 and 50° as shown by Figure S18, indicating that oxygen content in the PTL does not change significantly when contact angle increased to 50°.

Existing commercial PTLs, such as sintered or fiber PTLs, have uniform morphology and pore size distribution through the thickness of the PTL (Leonard et al., 2020). These PTLs also have lower through-thickness vs. in-plane tortuosities, essentially eliminating the possibility of oxygen front merging in plane in the middle of the PTL. The periodic waveform in this study also enables effective water delivery to the catalyst sites. Good in-plane transport properties, as shown in this study, can eliminate oxygen accumulation under the lands. It is possible to tailor the Ti-based PTL morphology to enable better in-plane transport by introducing gradient in particle sizes through the thickness of the PTL or using the fiber-based Ti PTLs and stacking two thinner layers instead of one thicker, although PTL-PTL contact resistances have to be accounted for.

Conclusions

In this study, X-ray CT and CFD were used to investigate oxygen transport in the PTLs of PEWEs. This study aimed to explain the preferential pathways of oxygen transport through the PTL. X-ray CT was performed using the in-house designed electrolyzer at different water feed rates (1-3 mlpm) and current densities (1 - 4 A/cm^2). Here, an acid-treated Freudenberg GDL was used as a model PTL on the anode because its pore size distribution most closely resembles conventional Ti-based sintered or fiber PTLs. Weka machine learning incorporated with the Z project method was able to quantify oxygen content throughout the PTLs via post-processing of *operando* X-ray CT scans.

The results show that more oxygen was present in the PTL near the catalyst layer (~27.5 %), compared to near the flow field (~7.5 %). Oxygen content in the PTL varied very little with either flow rate or current density, within the studied range. In addition, the oxygen content exhibited spatial periodicity, with peaks appearing at approximately 400 μm. These peaks range from 12 % oxygen content to a height of 25 % oxygen content. These findings are novel, as this is the first time oxygen content has been directly observed and quantified on a pore scale with direct observations.

The CFD model was able to correctly elucidate the oxygen content in the PTL as a waveform. However, the model predicted a period of 200 μm instead of experimentally observed 400 μm. The difference between the experimental and the modeling results, we believe, is due to the limitations in the implementation of bubble nucleation and growth in the CFD model. Overall, oxygen transport in this hydrophilic/aerophobic PTL is guided by pore size distribution of the PTL. Oxygen will transport through the large voids first before filling smaller voids. Thus, once the pathway through the thickness of the PTL is established, oxygen bubbles will preferentially follow the pathway and no new pathways will be introduced within the current densities range studied here. The high in-plane transport properties of the PTL (tortuosity of 1.3) compared to the through-plane (tortuosity of 1.8) enable oxygen to merge in the middle of the PTL and form the waveform. This periodic waveform has not been previously observed, and we believe this is due to the fact that commercial Ti PTLs have better through-plane than in-plane transport properties and thus merging of the oxygen pathways will not occur.

Since oxygen tends to take preferential pathways through the PTL, one can rationally design PTLs for selective water transport in and oxygen removal out. This can be achieved by either tailoring pore sizes or wettability. Hydrophobic PTL patterning will enable oxygen transport from the PTL at low resistance; however, water transport will be impeded. Gradient in porosity (Lettenmeier et al., 2017) in a hydrophilic PTL can direct oxygen transport, as oxygen will transport along the large voids. If MPLs are to be designed (Schuler et al., 2020), we believe introduction of cracks into the MPL can help with oxygen removal. Similar to this study, providing a high-porosity band in the middle of the PTL can help merge oxygen bubbles into a single channel, minimizing the area of the PTL for oxygen removal and providing more area within the PTL for water transport. The solutions suggested here can be expensive and will improve mass transport at high current densities (>2 A/cm^2). The voltage gains due to improved PTL transport properties have to be assessed with respect to the cost of production of advanced PTLs.

Limitations of the Study

Our work has demonstrated new findings in oxygen transport behavior in porous transport layers of PEWEs by using *operando* X-ray CT in combination with the LBM simulation. The spatially periodic oxygen front has been observed in this study for the first time. The study was applied to a single type model PTL. Additional investigations are needed to generalize the findings and to ensure that these are translatable across

the families of the PTLs. Future modeling study needs to incorporate the temperature effects and electrochemical kinetics to better capture transport effects on the oxygen transport behavior inside the PTLs.

Resource Availability

Lead Contact

Further information and requests for resources should be directed to and will be fulfilled by the Lead Contact, Iryna V. Zenyuk (Iryna.zenyuk@uci.edu).

Materials Availability

This study did not use or generate any reagents.

Data and Code Availability

This published article includes all data sets generated or analyzed during this study. The imaging data that support the figures and plots in this work are available from the lead contact upon reasonable request.

METHODS

All methods can be found in the accompanying Transparent Methods supplemental file.

SUPPLEMENTAL INFORMATION

Supplemental Information can be found online at https://doi.org/10.1016/j.isci.2020.101783.

AUTHORS CONTRIBUTION

P.S., M.O'B., and I.V.Z. analyzed the data and prepared the manuscript. D.K. and I.V.Z. designed the operando hardware and experiments. M.O'B. and I.V.Z. carried out all the experiments. D.Y.P. helped set up experiments and X-ray CT beamline. P.S. and S.S. designed and carried out the modeling study. C. C., K.E.A., N.D., and I.V.Z. defined the experimental approach and supervised. All authors contributed to the discussion and analysis of the data, as well as the editing of the manuscript.

DECLARATION OF INTERESTS

The authors declare no competing interests.

REFERENCES

Abdin, Z., Webb, C.J., and Gray, E.M. (2015). Modelling and simulation of a proton exchange membrane (PEM) electrolyser cell. Int. J. Hydrogen Energy 40, 13243–13257.

Babic, U., Suermann, M., Büchi, F.N., Gubler, L., and Schmidt, T.J. (2017). Critical review—identifying critical gaps for polymer electrolyte water electrolysis development. J. Electrochem. Soc. 164, F387–F399.

Bender, G., Carmo, M., Smolinka, T., Gago, A., Danilovic, N., Mueller, M., Ganci, F., Fallisch, A., Lettenmeier, P., Friedrich, K.A., et al. (2019). Initial approaches in benchmarking and round robin testing for proton exchange membrane water electrolyzers. Int. J. Hydrogen Energy 44, 9174–9187.

Carmo, M., Fritz, D.L., Mergel, J., and Stolten, D. (2013). A comprehensive review on PEM water

electrolysis. Int. J. Hydrogen Energy 38, 4901–4934.

Dedigama, I., Angeli, P., Ayers, K., Robinson, J.B., Shearing, P.R., Tsaoulidis, D., and ans Brett, D.J.L. (2014). In situ diagnostic techniques for characterisation of polymer electrolyte membrane water electrolysers - flow visualisation and electrochemical impedance spectroscopy. Int. J. Hydrogen Energy 39, 4468–4482.

Fornaciari, J.C., Gerhardt, M.R., Zhou, J., Regmi, Y.N., Danilovic, N., Bell, A.T., and Weber, A.Z. (2020). The role of water in vapor-fed proton-exchange-membrane electrolysis. J. Electrochem. Soc. https://doi.org/10.1149/1945-7111/ab9b09.

García-Valverde, R., Espinosa, N., and Urbina, A. (2012). Simple PEM water electrolyser model and experimental validation. Int. J. Hydrogen Energy 37, 1927–1938.

Han, B., Mo, J., Kang, Z., and Zhang, F.Y. (2016). Effects of membrane electrode assembly properties on two-phase transport and performance in proton exchange membrane electrolyzer cells. Electrochim. Acta 188, 317–326.

Kadyk, T., Bruce, D., and Eikerling, M. (2016). How to enhance gas removal from porous electrodes? Sci. Rep. 6, 1–14.

Kang, Z., Mo, J., Yang, G., Li, Y., Talley, D.A., Han, B., and Zhang, F.Y. (2017). Performance modeling and current mapping of proton exchange membrane electrolyzer cells with novel thin/tunable liquid/gas diffusion layers. Electrochim. Acta 255, 405–416.

Kang, Z., Yang, G., Mo, J., Yu, S., Cullen, D.A., Retterer, S.T., Toops, T.J., Brady, M.P., Bender, G., Pivovar, B.S., et al. (2018). Developing titanium micro/nano porous layers on planar thin/tunable LGDLs for high-efficiency hydrogen production. Int. J. Hydrogen Energy 43, 14618–14628.

Kim, P.J., Lee, C., Lee, J.K., Fahy, K.F., and Bazylak, A. (2020). In-plane transport in water electrolyzer porous transport layers with through pores. J. Electrochem. Soc. 167, 124522.

Lee, C., Lee, J.K., Zhao, B., Fahy, K.F., and Bazylak, A. (2020a). Transient gas distribution in porous transport layers of polymer electrolyte membrane electrolyzers. J. Electrochem. Soc. 167, 024508.

Lee, C.H., Hinebaugh, J., Banerjee, R., Chevalier, S., Abouatallah, R., Wang, R., and Bazylak, A.

(2017). Influence of limiting throat and flow regime on oxygen bubble saturation of polymer electrolyte membrane electrolyzer porous transport layers. Int. J. Hydrogen Energy 42, 2724–2735.

Lee, C.H., Lee, J.K., Zhao, B., Fahy, K.F., LaManna, J.M., Baltic, E., Hussey, D.S., Jacobson, D.L., Schulz, V.P., and Bazylak, A. (2020b). Temperature-dependent gas accumulation in polymer electrolyte membrane electrolyzer porous transport layers. J. Power Sourc. 446, 227312.

Leonard, E., Shum, A.D., Danilovic, N., Capuano, C., Ayers, K.E., Pant, L.M., Weber, A.Z., Xiao, X., Parkinson, D.Y., and Zenyuk, I.V. (2020). Interfacial analysis of a PEM electrolyzer using X-ray computed tomography. Sustain. Energy Fuels 4, 921–931.

Leonard, E., Shum, A.D., Normile, S., Sabarirajan, D.C., Yared, D.G., Xiao, X., and Zenyuk, I.V. (2018). Operando X-ray tomography and sub-second radiography for characterizing transport in polymer electrolyte membrane electrolyzer. Electrochim. Acta 276, 424–433.

Lettenmeier, P., Kolb, S., Sata, N., Fallisch, A., Zielke, L., Thiele, S., Gago, A.S., and Friedrich, K.A. (2017). Comprehensive investigation of novel pore-graded gas diffusion layers for high-performance and cost-effective proton exchange membrane electrolyzers. Energy Environ. Sci. 10, 2521–2533.

Lopata, J., Kang, Z., Young, J., Bender, G., Weidner, J.W., and Shimpalee, S. (2020). Effects of the transport/catalyst layer interface and catalyst loading on mass and charge transport phenomena in polymer electrolyte membrane water electrolysis devices. J. Electrochem. Soc. 167, 064507.

Mazloomi, K., and Gomes, C. (2012). Hydrogen as an energy carrier: prospects and challenges. Renew. Sustain. Energy Rev. 16, 3024–3033.

Sattari, E., Zanous, S.P., Farhadi, M., and Mohamad, A. (2020). Numerical investigation of the vapor bubble's scenarios passing through aerophobic/aerophilic porous structures using lattice Boltzmann method. J. Power Sourc. 454, 227929.

Schuler, T., Ciccone, J.M., Krentscher, B., Marone, F., Peter, C., Schmidt, T.J., and Büchi, F.N. (2020). Hierarchically structured porous transport layers for polymer electrolyte water electrolysis. Adv. Energy Mater. 10, 1–12.

Schuler, T., Schmidt, T.J., and Büchi, F.N. (2019). Polymer electrolyte water electrolysis: correlating performance and porous transport layer structure: Part II. Electrochemical performance analysis. J. Electrochem. Soc. 166, F555–F565.

Seweryn, J., Biesdorf, J., Schmidt, T.J., and Boillat, P. (2016). Communication—neutron radiography of the water/gas distribution in the porous layers of an operating electrolyser. J. Electrochem. Soc. 163, F3009–F3011.

Suermann, M., Schmidt, T.J., and Buchi, F.N. (2015). Investigation of mass transport losses in polymer electrolyte electrolysis cells. ECS Trans. 69, 1141–1148.

Suermann, M., Takanohashi, K., Lambirac, A., Schmidt, T.J., and Büchi, F.N. (2017). Influence of operating conditions and material properties on the mass transport losses of polymer electrolyte water electrolysis. J. Electrochem. Soc. 164, F973–F980.

Wang, J., Ji, L., Teng, X., Liu, Y., Guo, L., and Chen, Z. (2019). Decoupling half-reactions of electrolytic water splitting by integrating a polyaniline electrode. J. Mater. Chem. A 7, 13149–13153.

Zlobinski, M., Schuler, T., Büchi, F.N., Schmidt, T.J., and Boillat, P. (2020). Transient and steady state two-phase flow in anodic porous transport layer of proton exchange membrane water electrolyzer. J. Electrochem. Soc. 167, 084509.

Supplemental Information

Observation of Preferential Pathways for Oxygen

Removal through Porous Transport Layers

of Polymer Electrolyte Water Electrolyzers

Pongsarun Satjaritanun, Maeve O'Brien, Devashish Kulkarni, Sirivatch Shimpalee, Cristopher Capuano, Katherine E. Ayers, Nemanja Danilovic, Dilworth Y. Parkinson, and Iryna V. Zenyuk

TRANSPARENT METHODS

Operando cell hardware design

Due to the rotation needed during x-ray CT experiment at the beamline, it was necessary to design an *operando* cell with the limitations associated with the beamlines in mind. The *operando* cell reported previously (Leonard et al., 2018), consists of four aluminum plates, two BPPs, two PTLs, a Teflon gasket, a CCM masked with Kapton tape, and compressed together with anodized aluminum bolts. The graphite BPPs (Fuel Cell Store, College Station, TX), were chosen as they do not attenuate significantly x-rays. Figure S3 shows an assembled and exploded view of the electrolyzer hardware used for x-ray CT imaging.

The aluminum plates and BPPs were machined to provide a 1 cm long vertical x-ray transparent window for imaging. The BPPs were machined with a micro-mill, and in addition to the x-ray transparent window have two parallel channels 1mm x 1mm in area as well as a 1 mm land between the two channels. The cells are first assembled by cutting out a 2 cm^2 piece of CCM and masking it to 1 cm^2 active area with 20 μm Kapton film. Next, the PTLs were cut slightly larger than the active are of the CCM, in order to ensure that the active area would be covered completely during operation. The hard-stop PTFE-reinforced fiberglass gaskets were used on anode and cathode side of the electrolyzer to achieve 20 % compression on the cathode and 50 % compression on the anode. Finally, the entire cell is assembled, with special attention payed to ensuring that the CCM is evenly compressed. Six anodized aluminum bolts with extra washers were used to compress the cell. Multimeter was used to measure cell resistance after the PEWE assembly. If the resistance was several ohms, it meant that the cell was shorted, and it had to be reassembled. The current collector leads were attached with bolts to the sides of the graphite plates that were machined to accommodate this addition. Then, the set-up is connected with tubing to a

syringe pump and electrically to a potentiostat, as well, as cartridge heaters and thermocouples to provide heat flux.

Electrochemical Characterization and Operation

Gamry 5000E potentiostat (Gamry Instruments, Warminster, PA) was used as a power supply and also was used for electrochemical characterization of PEWEs. Liquid water (deionized (DI) water) was supplied on the anode side via a syringe pump (Harvard Apparatus, Holliston, MA). The syringe was filled with 40 mL of deionized water and connected to the cell via 1/8" tubing at the bottom inlet of the anode; another 1/8'' tube was connected to the outlet to collect unreacted water. The heat flux was applied with two cartridge heaters. The K-type thermocouples measured temperature on the top of the aluminum plates. A PID controller was used to control temperature of the PEWE (Leonard et al., 2020, 2018). Once the electrolyzer was loaded onto the beamline stage, water was introduced and the cell was heated for 30 minutes at 60°C to ensure that temperature was stable. Then, five polarization curves were collected between open circuit voltage (OCV) and maximum current density of 5 A/cm^2 at 20 mV/s as a break-in procedure and electrochemical impedance spectroscopy (EIS) was collected too. Then, a tomography scan was performed at OCV in order to get a background scan for future reference and to examine the alignment of the layers within the PEWE. Next the potentiostat was set to the desired current density and the tomography scans were collected. The experiments varied from constant currents of 1 to 4 A/cm^2, and water flow-rate of 1 to 3 milliliter per minute (mlpm) in increments of 1 A/cm^2 and 1 mlpm for current and water flow-rate, respectively. After each tomography scan, a polarization curve and EIS experiments were performed to check that the ohmic resistance was still within an acceptable range.

Image Processing and Visualization

The tomographic reconstructions were done utilizing TomoPy and the Grideric algorithm (De Carlo et al., 2014; Dowd et al., 1999; Pelt et al., 2016). The description of the reconstruction process in detail was discussed in our previous publications (Serov et al., 2018; Shum et al., 2017). In order to reduce the image stack size, the stacks were converted from 32-bit to 8-bit utilizing a JavaScript in Fiji/ImageJ (Schneider et al., 2012). The MATLAB plugin TauFactor (Cooper et al., 2016) was used to calculate porosity and tortuosity of segmented PTL layers. Pore size distribution (PSD) was defined using the BoneJ (Doube et al., 2010) available in ImageJ/Fiji. It should be noted that for every image stack they had to be converted using the same grayscale range so that each stack could be comparable to one another during further data analysis.

Machine learning for image processing

Machine learning was an integral part of this study to segment oxygen within the PTLs. The PTLs feature three phases: fiber, water and oxygen. One approach, that is conventionally is being used in a fuel cell community, is to obtain a reference scan at the OCV condition, segment fibers from this scan and then subtract the fibers to reduce the problem from the three phases (water, pores and fibers) to two phases (water and pores)(Alrwashdeh et al., 2017; Shrestha et al., 2020; Zenyuk et al., 2016, 2015). This approach is more difficult to implement for the electrolyzers studied here. First, at the OCV the images feature water and fiber because the dry scan will not be helpful for segmentation due to thick membrane swelling when water is introduced. The fiber and water in this study have very similar grey-scale values and hence only oxygen was thresholded, keeping water and fiber as a single phase. Although the segmentation problem is reduced to two phases, the oxygen (pore) phase has significant grey-scale values variation and hence regular segmentation algorithms introduced significant error.

The machine learning software was an ImageJ package the Waikato environment for knowledge analysis (Weka); it is an open-source plug-in specifically created for the classification of large sets of images (Witten et al., 2011). As it is a supervised machine learning algorithm, it requires the user to select and categorize the areas of interest on a given image. In the case of this study, oxygen content versus non-oxygen areas was of the most importance. The area of interest was selected from the stacks- i.e. the set of slices containing images of the PTL- and were adjusted so that the brightness and contrast were the same for every new stack.

After adjusting the brightness and contrast, a single stack was opened in the Weka interface. From there, selections from slices from the beginning, middle and end of the stack were classified. After classifying the slices of interest, the algorithm was used, and a classified stack was produced. The accuracy of the first run was lacking, and therefore multiple runs are needed before the accuracy of the algorithm is sufficient; the accuracy is easily determined by comparing the classified slices with the original slices by eye. In Figure S4, examples of slices pre and post segmentation training in Weka are shown, where the red areas are classified as oxygen and the green areas are either fiber or water. In order to achieve the level of accuracy required, the classifier was trained four times, with more slices classified by hand in order to further increase the accuracy. This iterative process was necessary, as the grayscale values between oxygen and non-oxygen areas in the PTLs were relatively close, thus making it difficult for the algorithm to differentiate between the two categories in the first two runs.

Once the algorithms were trained, the next step was to apply the final algorithm to the entire stack. This was done by splitting the original stack containing the PTL into two and analyzing them with the same algorithm in parallel. This was done on 64 Gb RAM computer stations and splitting stack in two of 2,000 images ensured higher computational efficiency. This

process was repeated for every test, resulting in a red and green image stack that was then converted into binary for processing and for the input with the z-project function in ImageJ. Z-project function is projecting an average of the oxygen content of the volume onto a single slice. An additional step taken prior to utilizing the z-project function was to collapse the pixel values to be between 0 and 1- this served two purposes: the first was to simplify the z-project calculations and the second is to make later interpretation in MATLAB easier. After processing, the resulting z-projects for the different tests were made into 3D meshes for both qualitative and quantitative analysis. The description of quantification of oxygen content in PTLs is given in SM. Here we briefly define oxygen content as:

$$O_2 \; content = \frac{V_{O_2}}{V_{tot}} \tag{1}$$

where, V_{O_2} is the volume of oxygen within selected region of interest and V_{tot} is the total volume of the region of interest. Thus, one can thing of oxygen content as a normalized volume fraction of oxygen within a selected volume.

Modeling

3D time-dependent simulations of oxygen transport inside the PTL for PEWE with the LBM multiphase flow model were run for this model electrolyzer. The Boltzmann transport equation was solved and used to predict the mass transport in the PTL. This model was adapted from LBM multi-scale fuel cell model (Satjaritanun et al., 2020) developed by some of the co-authors. The Boltzmann transport equations related to the electrochemical devices modeling, such as fuel cell are discussed in LBM section and previous publications (Satjaritanun et al., 2020, 2018, 2017). The PTL sample used in this model was treated Freudenberg GDL. The computational lattice size was 1.00 μm for this PTL, which derives from the grid (lattice element size)

independence study, as discussed in the SM. The computational domain has a size of 3,000 x 3,000 x 320 μm^3. The anode side of the electrolyzer was assumed to be the control in this model. The co-flow condition was applied in both channels of this model electrolyzer.

LBM used the lattice node as a unit element to replace the typical computational meshes for its direct numerical simulation. According to the size of geometry, the time step was set to 0.001 microsecond per time step. Through this modeling, the transport behavior and characteristics of the reactant liquid water and product, such as oxygen gas were investigated under various operating conditions similar to the experimental set up. Two simulations were run: 1) with constant oxygen flux as a boundary condition at the catalyst layer corresponding to constant current density and 2) the sinusoidal wave oxygen flux boundary at the catalyst layer with period of 400 μm to attempt to reproduce oxygen concentration observed experimentally. The inlet mass flow conditions of water in the PTL were used the same as in the experiment. The surface wettability of PTL was assumed to be uniform and constant across the entire surface at 10 degrees. The model was run in isothermal mode. The software XFlow 2020 Refresh 1 Beta (Build 108.07) was used to perform the calculations.

Lattice Boltzmann Method (LBM)

LBM was chosen to perform the numerical analysis in this work. It is one of the most powerful techniques for computational fluid dynamics (CFD) for a wide variety of complex turbulent flow problems including multiphase flow and free surface models with complex geometries, such as PTL in the electrolyzer. This method uses the concept of streaming and collision of particles which incorporates the physics of microscopic and mesoscopic processes so that the macroscopic averaged properties obey the desired macroscopic equations (Frisch et al.,

1986; McNamara and Zanetti, 1988; Chen and Doolen, 1998). The transport equation of this method is shown below:

$$f_i(\vec{x} + \vec{e}_i \Delta t, t + \Delta t) - f_i(\vec{x}, t) = \Omega_i(f_1(\vec{x}, t), \dots, (f_b(\vec{x}, t)), \quad i = 1, \dots, b \qquad \text{(S.1)}$$

where f_i is the particle distribution function in direction i, $\vec{x}$ is the lattice node, $\vec{e}_i$ is the particle discrete set of velocities, t is the discrete times, Δt is the constant time step, Ω_i is the collision operator, and b is the probability distribution function of the particle distribution function mentioned above. As in the continuum Boltzmann equation, macroscopic variables, such as density ρ and velocity $\vec{u}$, can be calculated as the moments of the density distribution function:

$$\rho = \sum_{i=1}^{b} f_i \qquad \text{(S.2)}$$

$$\rho\vec{u} = \sum_{i=1}^{b} f_i \, \vec{e}_i \qquad \text{(S.3)}$$

The macroscopic fluid pressures are calculated from the equation of stage:

$$P = \rho c_s^2 \qquad \text{(S.4)}$$

The multiscale Chapman-Enskog expansion gives us the relation between the macroscopic kinematic viscosity (ν) and the relaxation parameter (τ):

$$\nu = c_s^2 \left(\tau - \frac{1}{2}\right) \qquad \text{(S.5)}$$

where c_s is the speed of sound. For the positive kinematic viscosity, $\tau > \frac{\Delta t}{2}$ is a required stability condition. In addition, therelaxation time should stay within the range 0.5-1.5. The value in this study is 0.5. The LBM makes use of statistical distribution function with real variables, conserving

the conservation of mass, momentum, and energy(Chen and Doolen, 1998). In this model, the collision operator can be approximated by the multiple relaxation time (MRT) as followed:

$$\Omega_i^{MRT} = M_{ij}^{-1}\hat{S}_{ij}\left(\mu_i^{eq} - \mu_i\right) \tag{S.6}$$

where the collision matrix $\hat{S}_{ij}$ is a b $\times$ b diagonal relaxation matrix, μ_i^{eq} is the equilibrium value of the μ_i, and M_{ij} is a b $\times$ b matrix, which transforms the distribution function to macro-scopic moment(Shan and Chen, 2007; d'Humieres, 2002). The collision operator is based on a multiple relaxation time scheme. However, as opposed to standard MRT, the scattering operator is implemented in central moment space. The relaxation process is performed in a moving reference frame by shifting the discrete particle velocities with the local macro-scopic velocity, naturally improving the Galilean invariance and the numerical stability for a given velocity set (Holman et al., 2012; Premnath and Banerjee, 2012). Analogically to Eqs (S.2) and (S.3), raw moments of the probability distribution function f can be defined as:

$$\mu_x k_y l_z m = \sum_i^b f_i e_{ix}^k e_{iy}^l e_{iz}^m \tag{S.7}$$

and the central moments can be defined as:

$$\tilde{\mu}_x k_y l_z m = \sum_i^b f_i (e_{ix} - u_x)^k \left(e_{iy} - u_y\right)^l (e_{iz} - u_z)^m \tag{S.8}$$

where k, l, and m are the orders of moments taken in x, y, and z directions, respectively, and e_{ix}, e_{iy}, and e_{iz} are the particle discrete set of velocities in x, y, and z directions, respectively. The raw moment order is therefore $k + 1 + m$. Denoting μ_i as a raw moment $\mu_x k_y l_z m$ of a given combination of k, l, and m. The relation between the PDFs and the raw moments can be defined as:

$$\mu_i = M_{ij}f_i \qquad \qquad \text{(S.9)}$$

The grid (lattice element size) independence study was tested. A voxel size of 0.5, 0.8, and 1.0 μm were compared to determine if the lattice size significantly affects liquid saturation levels. These simulations were computed with an operating condition of 1 A/cm^2 with the water flow-rate of 2 mlpm. The results show that there is minimal change in the amount of oxygen present inside each simulation. So, a lattice size of 1.0 microns was acceptable.

Model assumption of oxygen bubbles transport in PTL

In general, before the oxygen forms bubbles, it is present in dissolved form, only once dissolved oxygen concentration reaches the critical value, then the oxygen starts forming bubbles (Kadyk et al., 2016). In this work, the oxygen gas form instead of dissolved form is used to define as the inlet boundary at the top wall boundary where the catalyst layer is located. In the top wall surface domain, the nucleation and growth of bubbles is considered without dissolved form of oxygen. The oxygen nucleation diameter was set at 1 μm, which is related to the lattice element diameter. Since the oxygen uniform flux is used, the nucleation density of 3,000 x 3,000 sites was applied to the simulation.

Table S1. Eotvos number calculation. Related to Figure 6.

Parameters	Value	Unit	Note
ρ_{water}	998	kg/m^3	Water density at 20 °C
ρ_{oxygen}	1.429	kg/m^3	Oxygen density at 20 °C
G	-9.81	m/s^2	Gravity
σ	0.0072	N/m	Surface tension of water at 20 °C
B	1.03E-05	m	Average pore radius
Eo	0.000136		Eotvos number
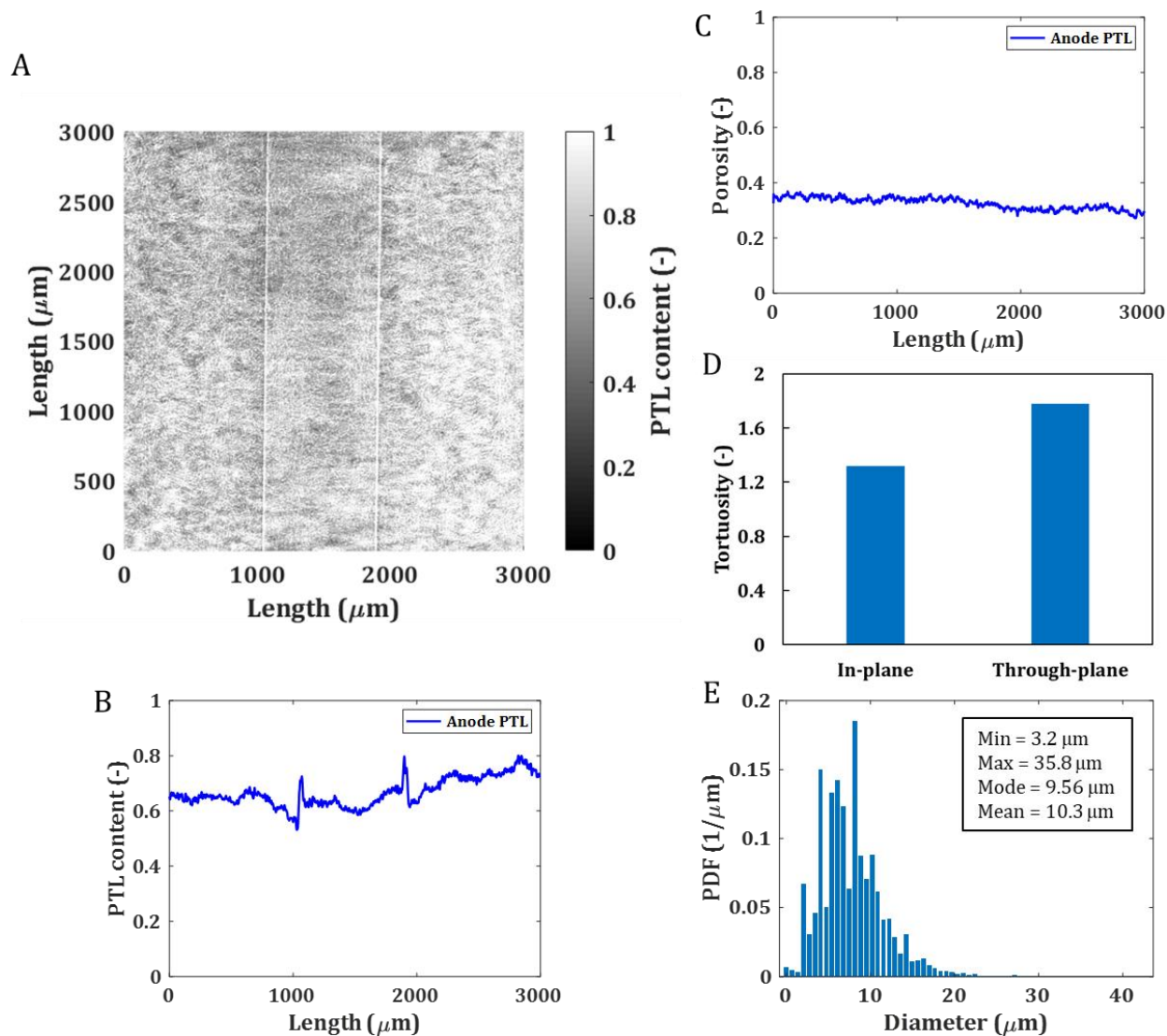
Figure S1. The morphological information about the PTLs used in this study.

(A) Z-project of the PTL content in anode side of PEM electrolyzer. (B) plot of PTL content along the length of the sample. (C) Porosity profile of anode PTL. (D) Tortuosity of anode PTL. (E) Pore size distribution of anode PTL. Related to Figure 1.
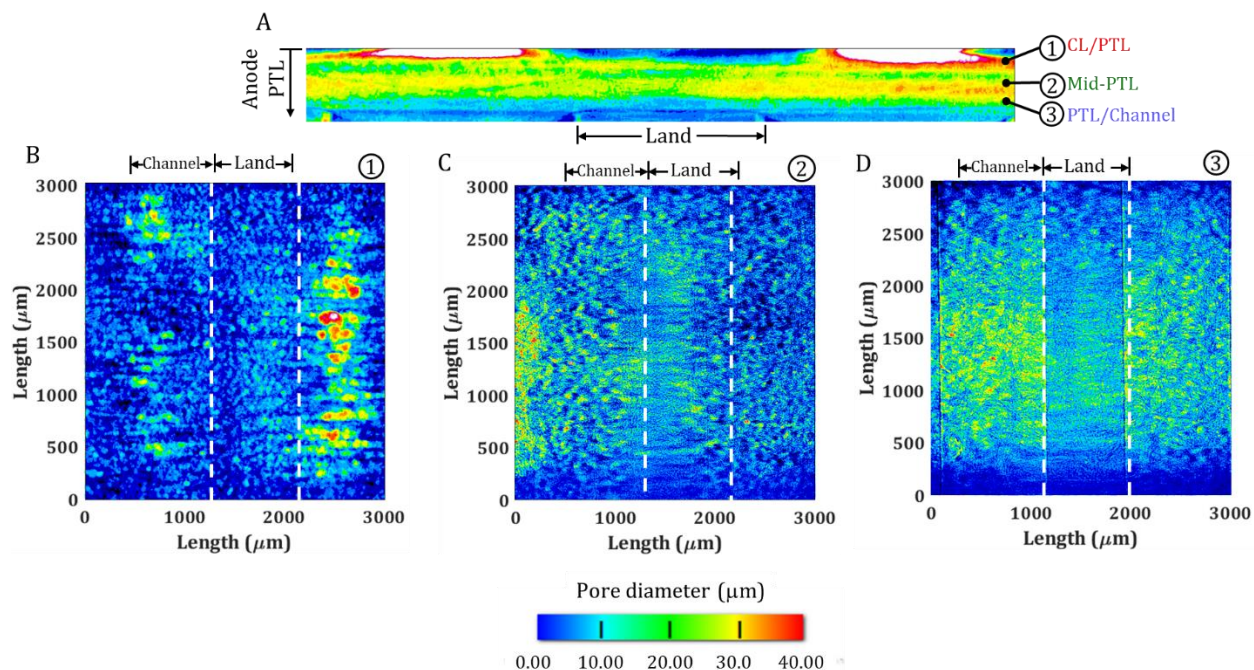
Figure S2. Spatially-resolved pore-size distributions of the PTL.

(A) Average pore size distribution for the PTL, (B) top one third corresponding to the PTL in contact with CL, (C) middle portion of the PTL, and (D) last one-third of the PTL in contact with channel. Related to Figure 1.
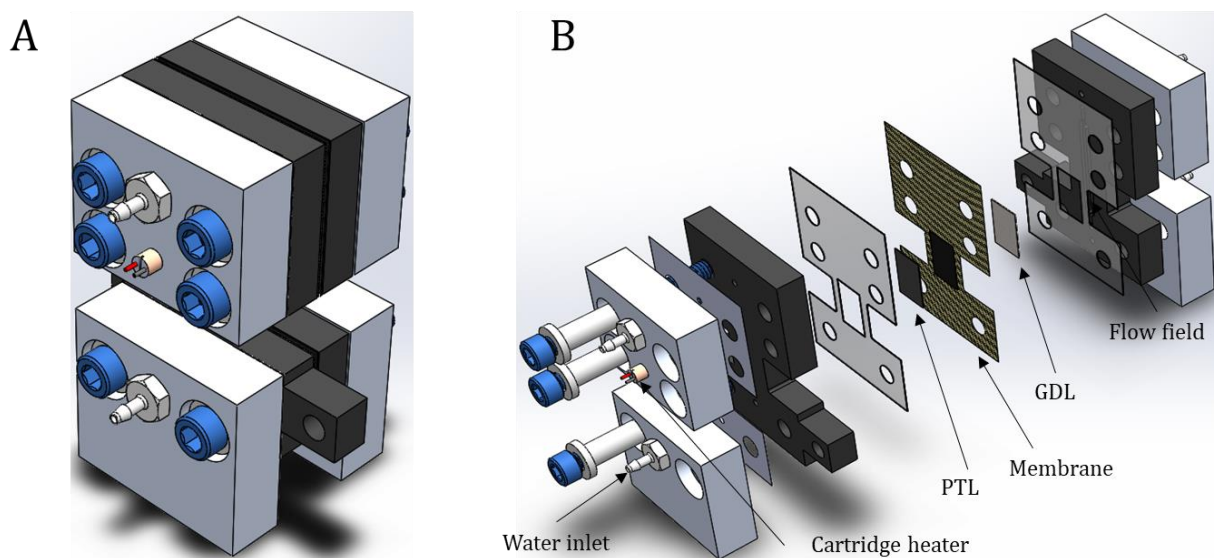
Figure S3. Solidworks drawings of the electrolyzer used for operando studies.

(A) the fully assembled PEM electrolyzer cell, and (B) the exploded view of the PEM electrolyzer cell, with the GDL, PTL and ionomer (PEM membrane). Related to Figure 1.
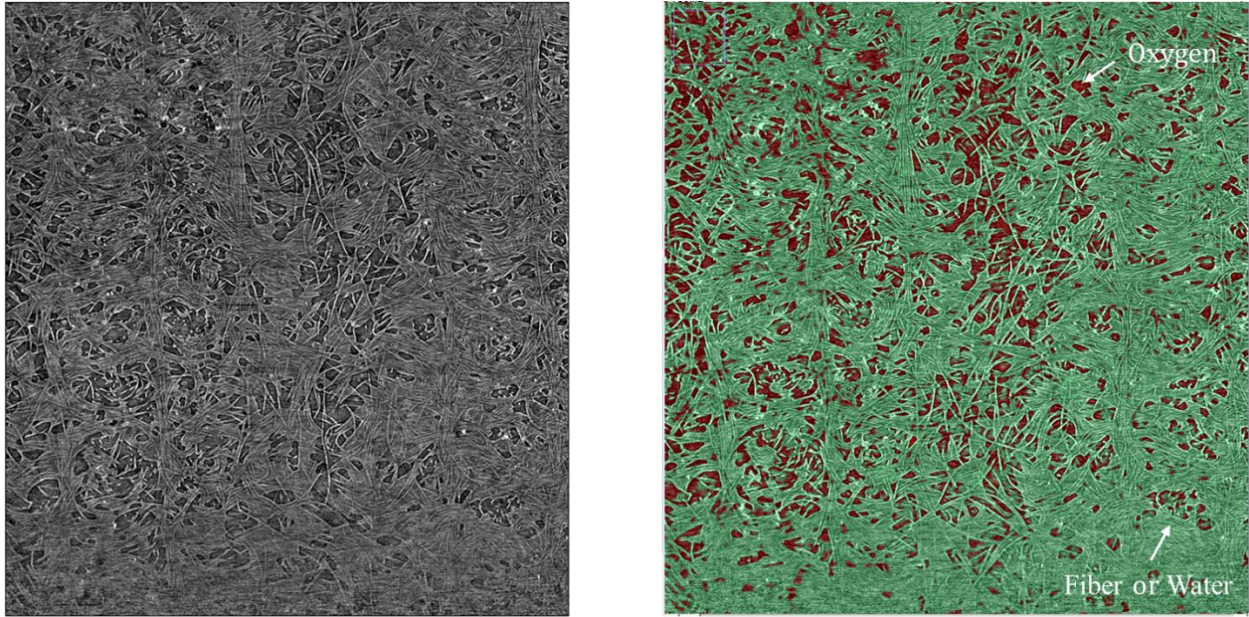
Figure S4. Image segmentation example.

Examples of images pre(left) and post(right) processing with Weka. Post processing, the image is segmented into areas of oxygen, in red, and areas or either water or fiber which is displayed as green. Related to Figure 1.
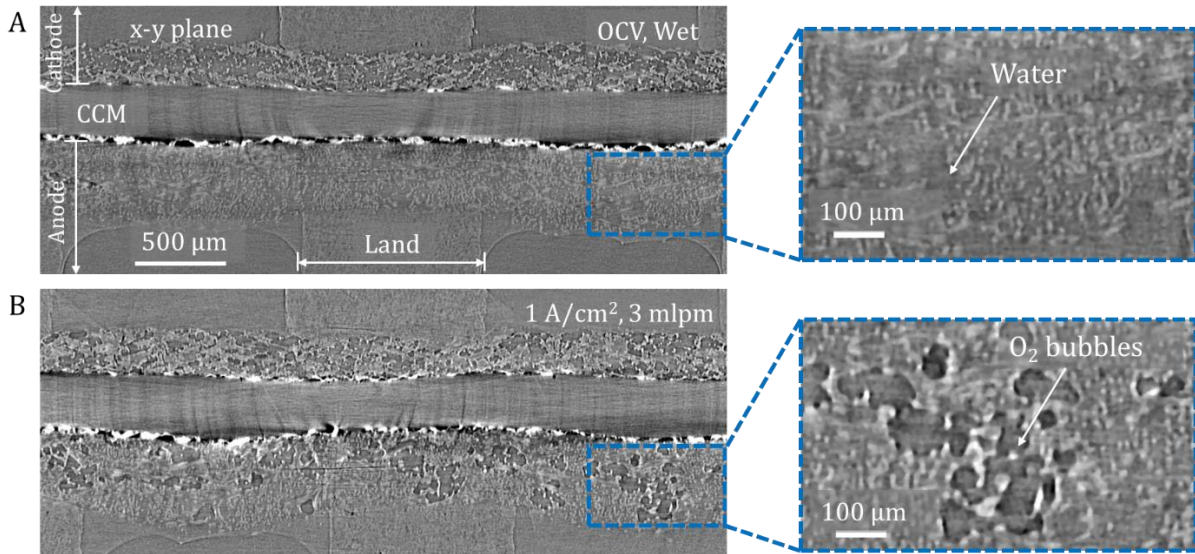
Figure S5. An illustration of water-filled and oxygen-filled PTLs.

(A) The x-y plane of an electrolyzer at OCV (GDL and PTL are saturated with water), and (B) The x-y plane of an electrolyzer at 1 A/cm², 3 mlpm, which presents the oxygen bubbles seen as voids within the PTL. Related to Figures 1 and 2.
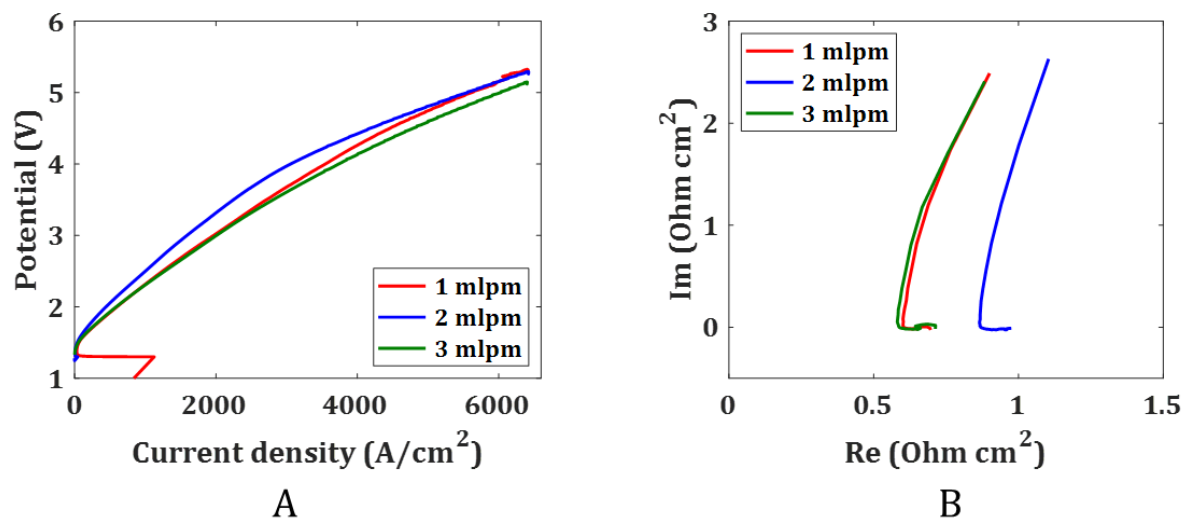
Figure S6. Electrochemical performance data for the operando electrolyzer.

(A) Polarization and (B) EIS of the cells prior to in-situ x-ray computed tomography. Related to Figure 3.

Figure S6A shows polarization curves, which are potential as a function of the applied current density. The polarization curves were recorded between 0 and 6 A/cm^2 and three water flow-rates 1, 2 and 3 mlpm. We observe similar polarization behavior between the three conditions, indicating that the water flow-rate did not have significant effect on electrolyzer performance. We also observe relatively high voltages (5 V at 5 A/cm^2). To explain this high potential we study Nyquist plot, shown by Figure S6b. From Figure S6B the real-axis intercept that corresponds to high-frequency resistance (HFR) of electrolyzer can be extrapolated to be 0.6 to 0.8 Ohms. At 5 A/cm^2, which is a high current, the voltage drop due to Ohmic loss for a cell with 0.6 Ohm will be 3 V. Thus a large contribution to the cell potential is Ohmic loss. The high HFR is due to limitations in the operando cell design, as graphite plate is used as a current collector and because it is porous it has limitations in terms of electric conductivity. Additionally, contact resistances between the graphite plate and Ti-PTL can be another sources of higher HFR. The Nafion 117 membrane with

the thickness of 180 μm is used in this work, which is also the reason for high HFR. 2 mlpm flow-rate showed higher HFR and also bit worse polarization behavior.
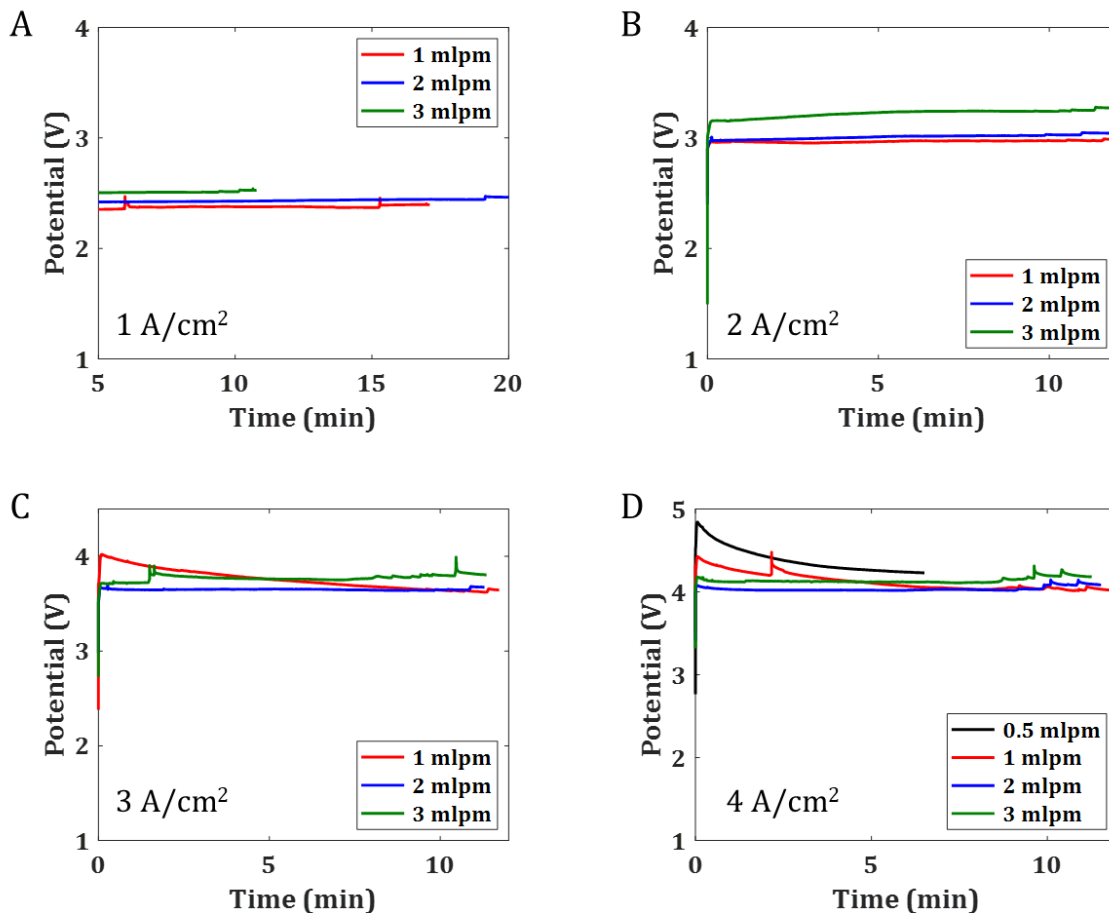

Figure S7. **Current holds during operando x-ray CT scan.**
(A) 1A/cm^2 through (D) 4A/cm^2, for each flow rate. Related to Figure 3.

Figure S7 shows the potential as a function of time across the applied current densities and water flowrates. The maximum current density used in this study was 4 A/cm^2. We varied the applied current density from 1 A/cm^2 to 4 A/cm^2. For each applied current density, the flowrate was varied from 1mlpm up to 3mlpm. Prior to imaging, the cells are conditioned and checked for performance. Figure S7A shows that for three flow-rates the potential was around 2.5 V for the

measuring time between 10 and 20 min. Figure S7b shows potential of the cell being around 3 A/cm^2 for the three water flowrates. For 3 and 4 A/cm^2, as shown by Figure S7C and S7D, respectively, we see initial increase in potential for water flowrates of 0.5 and 1 mlpm but eventual decay in potential with time for this water flowrate. This is indicative that there is some kind of relaxation in the electrolyzer and better performance is achieved at lower water flow-rate with time. Overall, the polarization curves and constant current holds suggest that electrolyzer performance is not significantly affected by water flow-rate.
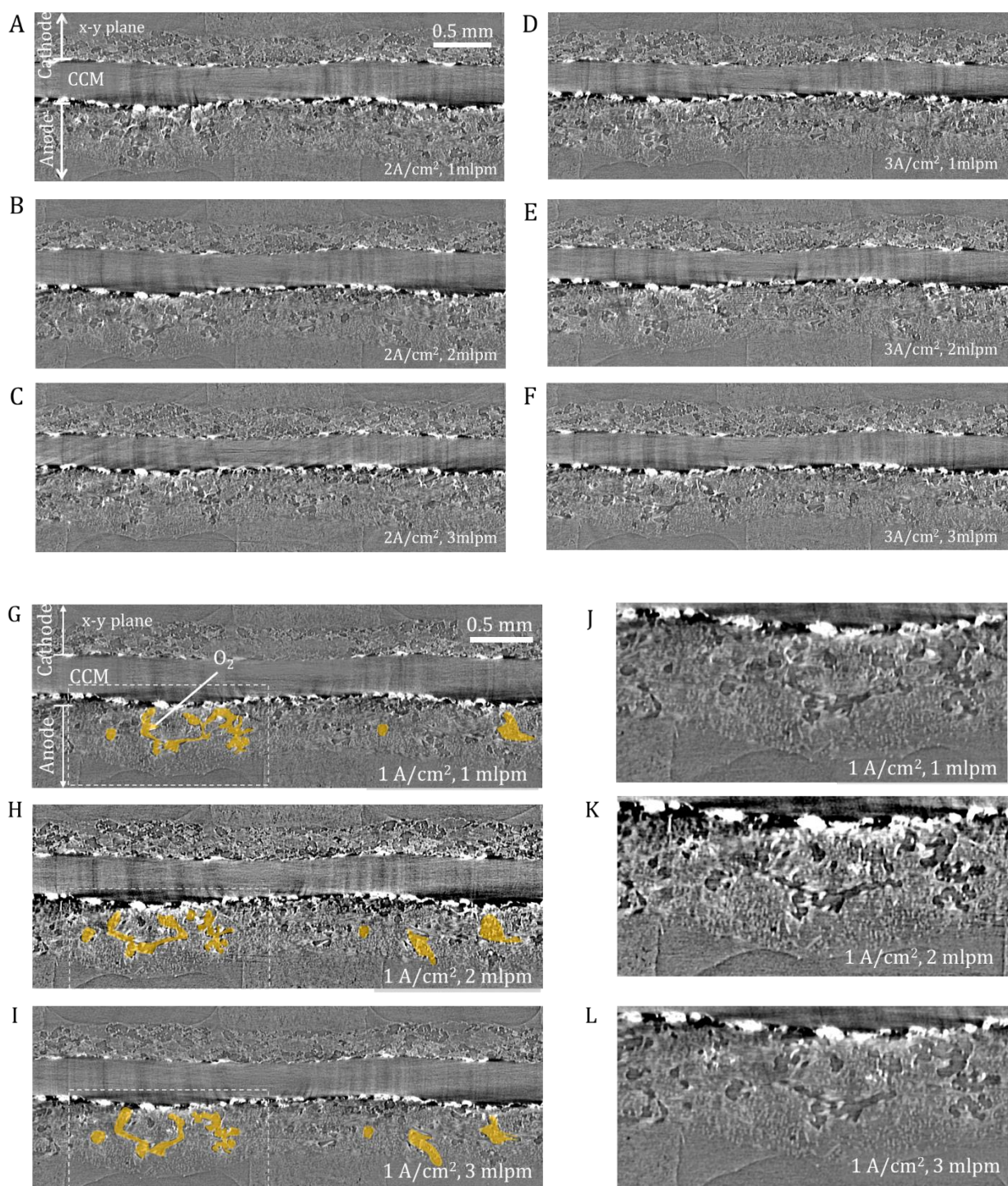
Figure S8. **Examples of grey-scale images for operando electrolyzers at varied current densities and water flow-rates.**

The x-y plane of the PEM electrolyzer during cell operation, where (A) 2A/cm², 1mlpm, (B) 2A/cm², 2mlpm, (C) 2A/cm², 3mlpm, (D) 3A/cm², 1mlpm, (E) 3A/cm², 2mlpm and (F) 3A/cm²,

3mlpm. The false-colored images (G-I) represent the oxygen pathways for 1 A/cm^2 current density and 1- 3 mlpm water flow-rate. The (J-L) images represent the zoomed-in portions from (G-I). Related to Figure 2.
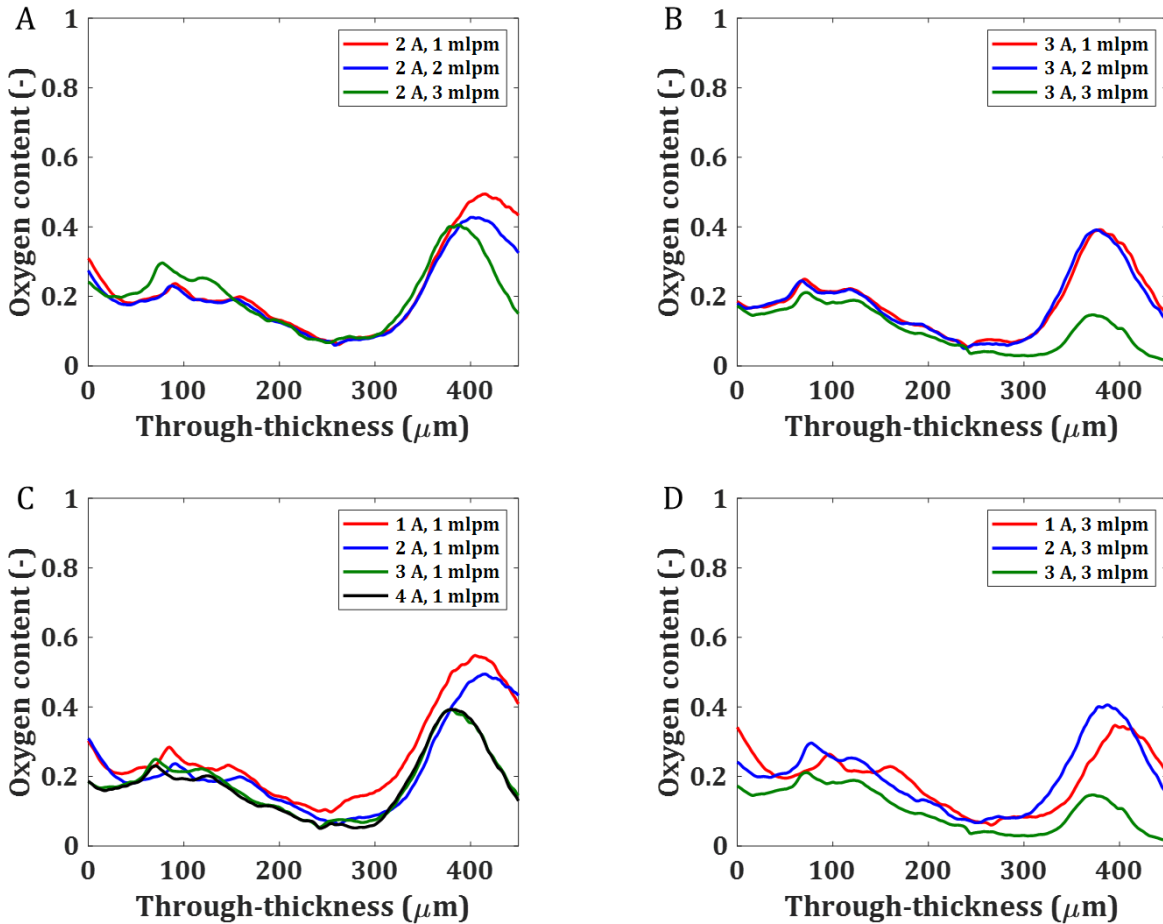
Figure S9. **Oxygen content as a function of through-thickness PTL location.**

(A) The comparison of oxygen content at 2 A/cm^2 with varied flowrates. (B) The comparison of oxygen content at 3 A/cm^2 with varied flowrates. (V) The comparison of oxygen content for varied current at constant flowrate of 1 mlpm. (D) The comparison of oxygen content for varied current at constant flowrate of 3 mlpm. Related to Figure 3.
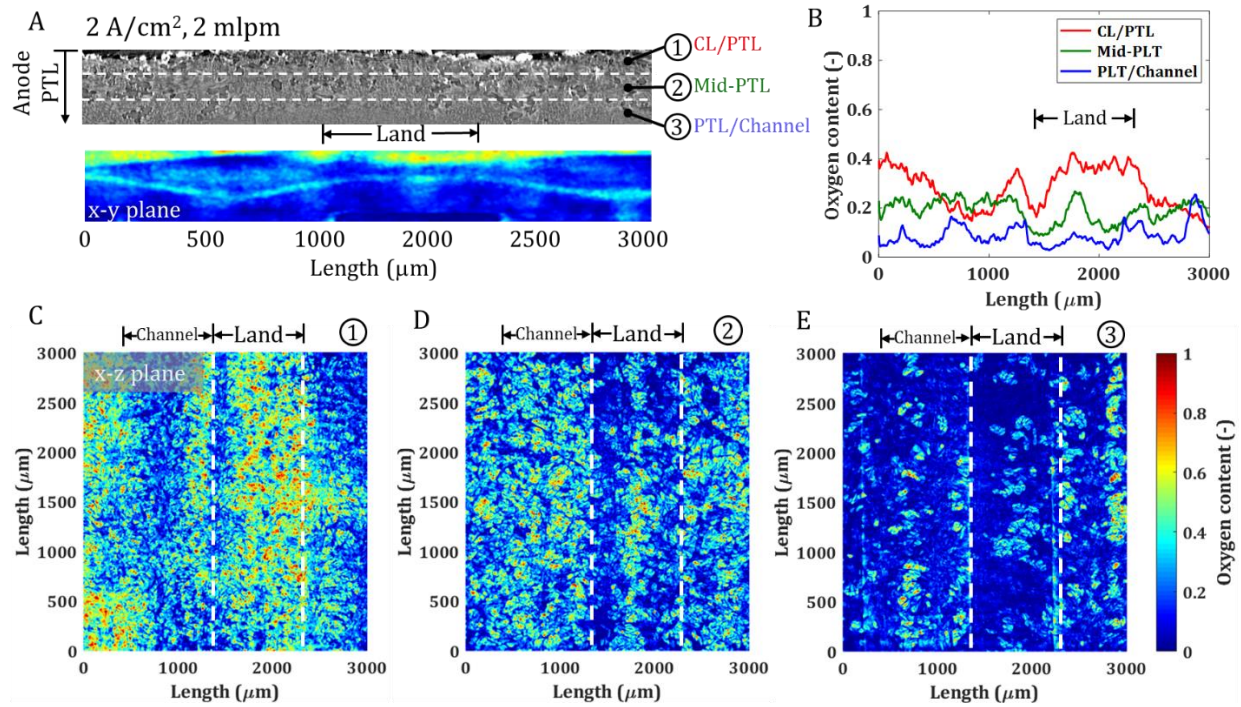
Figure S10. The comparison of oxygen content within the different portions of PTL at the operating condition of 2 A/cm², 2 mlpm.

(A) Top, 1/3 portions of PTL that located CL/PTL interface, Middle of PTL, and PTL/channel interface, and bottom, 2D oxygen content of PTL at x-y plane by using Z-project method. (B) Oxygen content comparison at different PTL portions. (C) Z-project of the oxygen content of the x-z plane at the CL and PTL interface. (D) Z-project of the oxygen content of the x-z plane at the middle PTL portion. (E) Z-project of the oxygen content of the x-z plane at the PTL and channel interface. Related to Figures 4 and 5.
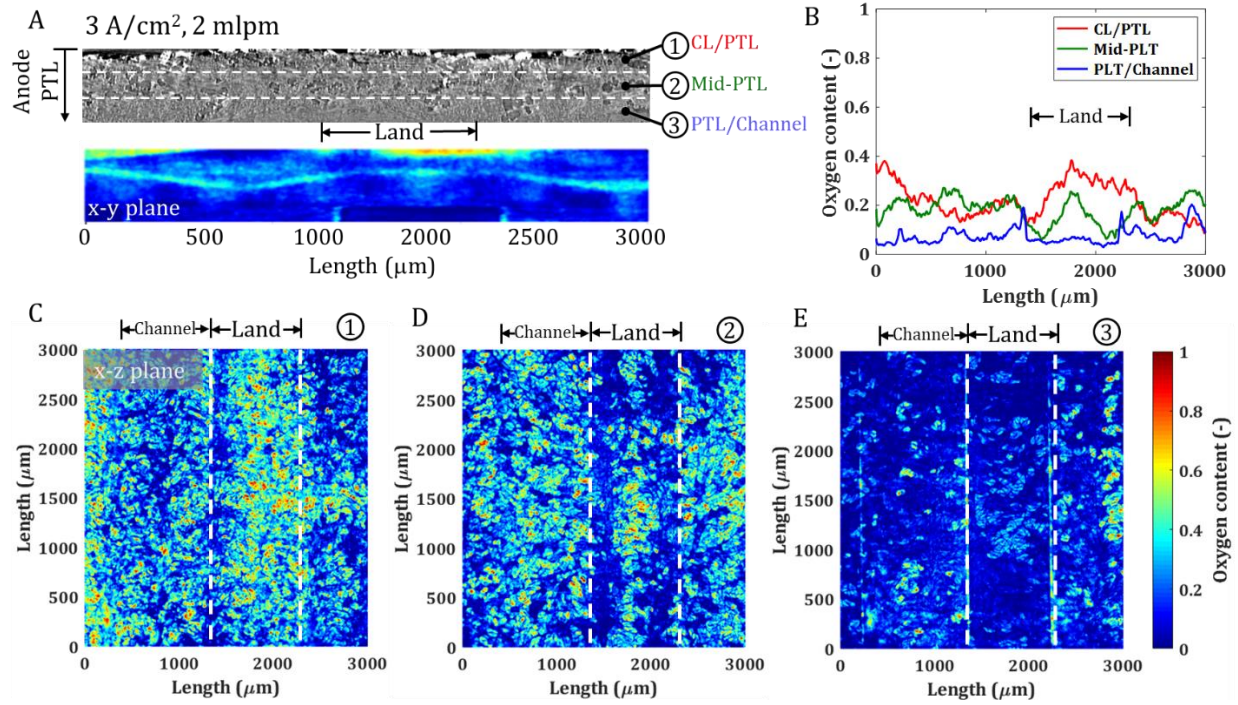
Figure S11. **The comparison of oxygen content within the different portions of PTL at the operating condition of 3 A/cm², 2 mlpm.**

(A) Top, 1/3 portions of PTL that located CL/PTL interface, Middle of PTL, and PTL/channel interface, and bottom, 2D oxygen content of PTL at x-y plane by using Z-project method. (B) Oxygen content comparison at different PTL portions. (C) Z-project of the oxygen content of the x-z plane at the CL and PTL interface. (D) Z-project of the oxygen content of the x-z plane at the middle PTL portion. (E) Z-project of the oxygen content of the x-z plane at the PTL and channel interface. Related to Figures 4 and 5.
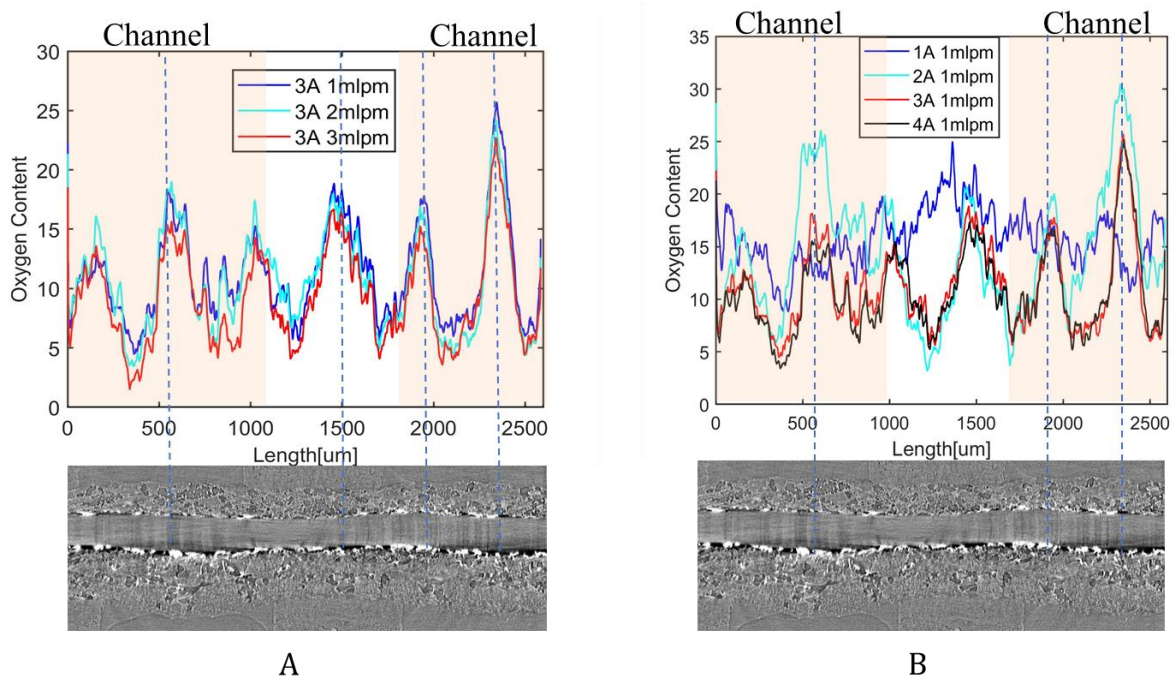
Figure S12. **Oxygen content measurements along the length of the PEM electrolyzer.**

In this plot (A) compared the same current density at different flowrates and (B) compared different current densities at the same flowrate. Related to Figures 4 and 5.

      Figure S12A shows oxygen in-plane concentration for 3 A/cm^2 and three flow-rates, whereas Figure S12B shows oxygen content in the PTL where the current densities varied but the water flowrate of 1 mlpm was constant. This data represents oxygen content in PTL near the land and channel locations, only 1/3 of PTL thickness was used to generate this data. The red dashed lines connect to the bright areas of the x-y plane cross-section below, where the bright areas correspond to the catalyst. Peaks in the oxygen content across the length of the PTL are observed periodically, regardless of the flowrate. The oxygen peaks appear every 400 μm. The peaks oxygen fractions varied from 12 to 25 %, whereas the oxygen fraction valleys varied from 2.5 to 7 %. Interestingly, that for 1 A/cm^2 and 1 mlpm the peaks in oxygen concentration are not pronounced and oxygen content varies between 15 and 20 %. As we mentioned before, at 1 A/cm^2 the cell was not fully conditioned and hence the results are different from the other results. Oxygen distribution

at 3 and 4 A/cm^2 shows virtually similar trend. What we can conclude that when exiting the PTL oxygen arranges into the channels that are 400 μm apart and then either is trapped under the land or leaves through the channel.
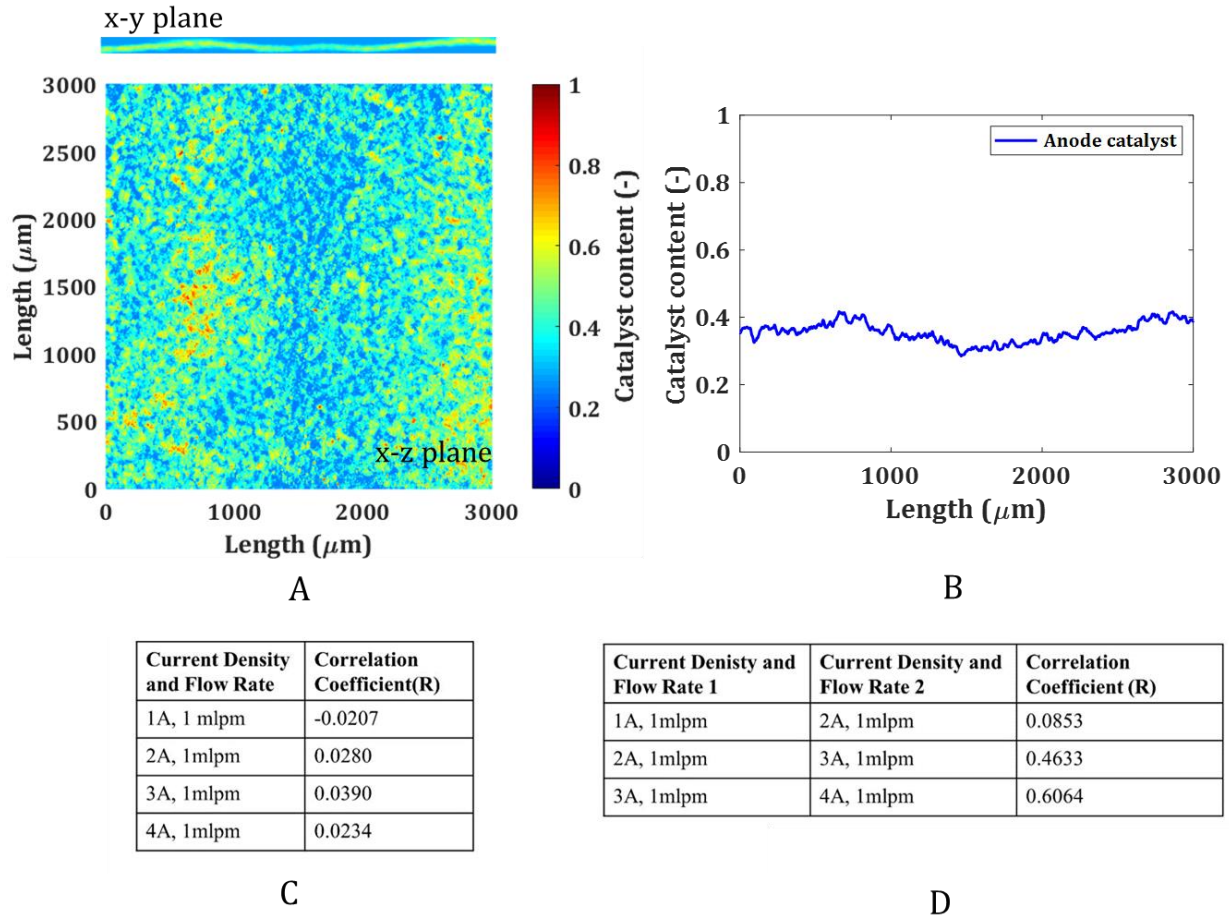

Figure S13. **Z-project of the catalyst content in anode side of PEM electrolyzer.**

(A) Catalyst content in the x-y plane (top) and in the x-z plane (bottom). (B) Plot of the catalyst content along the length of the sample. (C) Details the correlation coefficients between the catalyst distribution and the different current densities. (D) comparing the current densities for the same flowrate for comparison to the correlation coefficients found for the catalyst vs current density. Related to Figures 4 and 5.

Figure S13C and S13D shows correlation coefficients between data of different current densities and also between oxygen content and catalyst distribution in the catalyst layer.

Correlation coefficient of 1 and -1 indicates that the two images match, whereas correlation of 0 indicates that there is no overlap. There was little to no correlation found between the catalyst distribution and the oxygen content, as correlation coefficients are blow 0.1. Therefore, there is likely another explanation for the periodicity of the oxygen content at the bottom of the PTL. This periodicity is perhaps due to oxygen taking preferential pathways as it exits the PTL, which would account for the apparent periodicity. Comparing the correlation coefficients for oxygen content between various current densities we observe strong correlation between 2 and 3 A/cm^2, and also 3 and 4 A/cm^2 but weak correlation between 1 and 2 A/cm^2. This is, as we already mentioned is due to the fact that electrolyzer was not yet conditioned well.

Aerophobic simulations with air-water contact angle of 170 degrees with periodic oxygen front

For the sinusoidal wave boundary model, the simulation applied the sinusoidal oxygen flux on the top of PTL, where the catalyst layer is located, as shown in SM, Figures. S13 and S14. The wave boundary was assigned to have a period of 400 μm to attempt to reproduce oxygen concentration observed experimentally. The simulation is able to capture and present the catalyst activity on and off, where the oxygen production in the experiment is formed as a wave near the catalyst surface. So, the oxygen is produced only when the catalyst is active, not on the entire surface of the top of PTL. There is an oxygen wave that appears near the catalyst layer similar to the experiment. Moreover, the simulation also shows the oxygen peaks appear every 500 μm, which is slightly higher than those observed in the experiment.
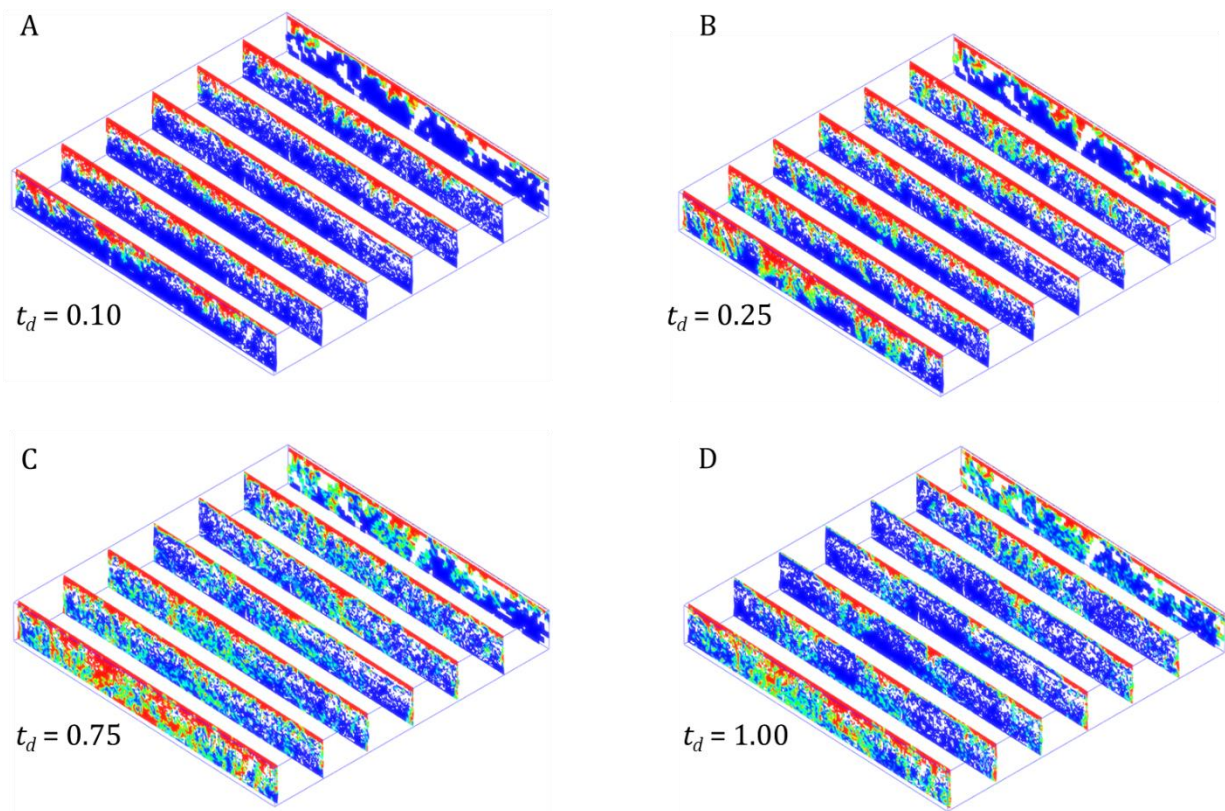
Figure S14. **Isometric view with cross section in the PTL sample that show time dependent CFD simulation of oxygen content distribution in the PTL at 1 A/cm^2 with the flow-rate of 2 mlpm.** This model applied the sinusoidal flux of oxygen on the top of PTL. The aerophobic of oxygen was defined between the surface of oxygen-water with the contact angle of 170 degree. Note that the dimension less time, $t_d = 1.0$ is the steady state time at 5 ms. Related to Figure 6.
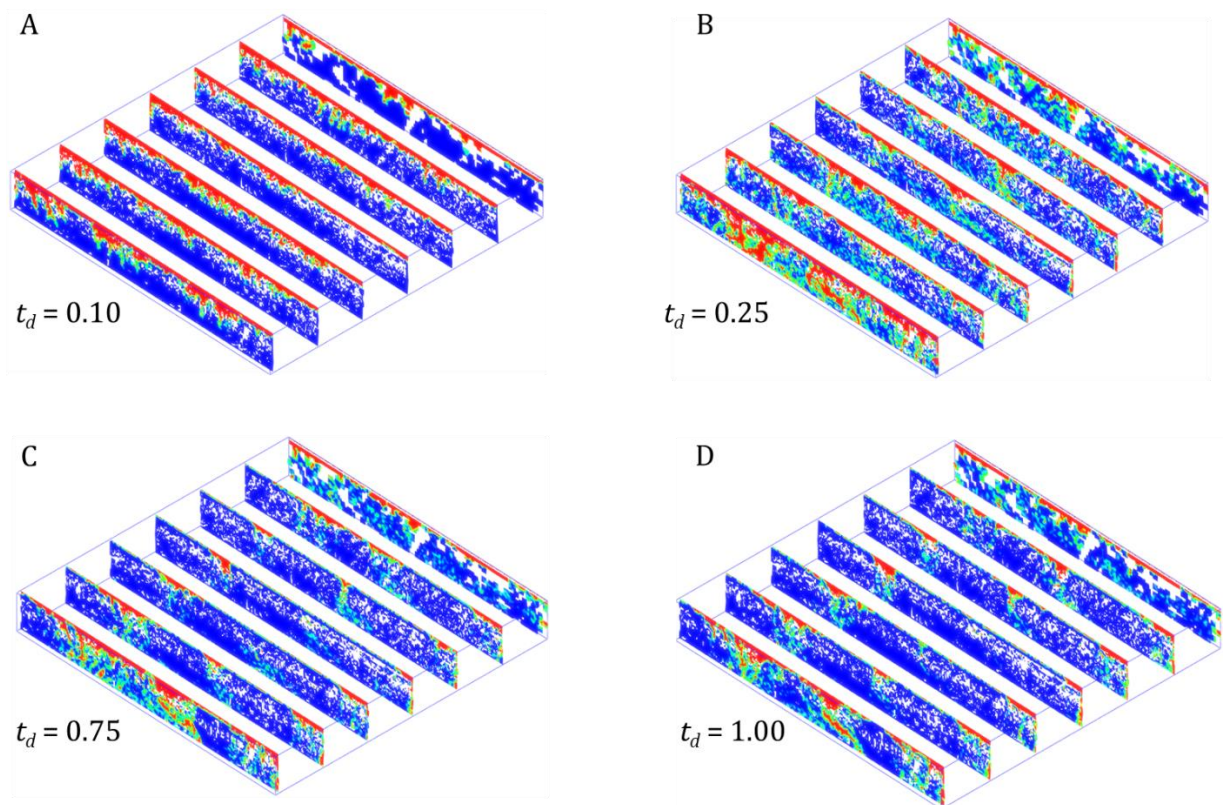
Figure S15. **Isometric view with cross section in the PTL sample that show time dependent CFD simulation of oxygen content distribution in the PTL at 4 A/cm^2 with the flow-rate of 2 mlpm.**

This model applied the sinusoidal flux of oxygen on the top of PTL. The aerophobic of oxygen was defined between the surface of oxygen-water with the contact angle of 170 degree. Note that the dimension less time, $t_d = 1.0$ is the steady state time at 5 ms. Related to Figure 6.

Aerophilic simulations with air-water contact angle of 10 degrees with constant oxygen flux
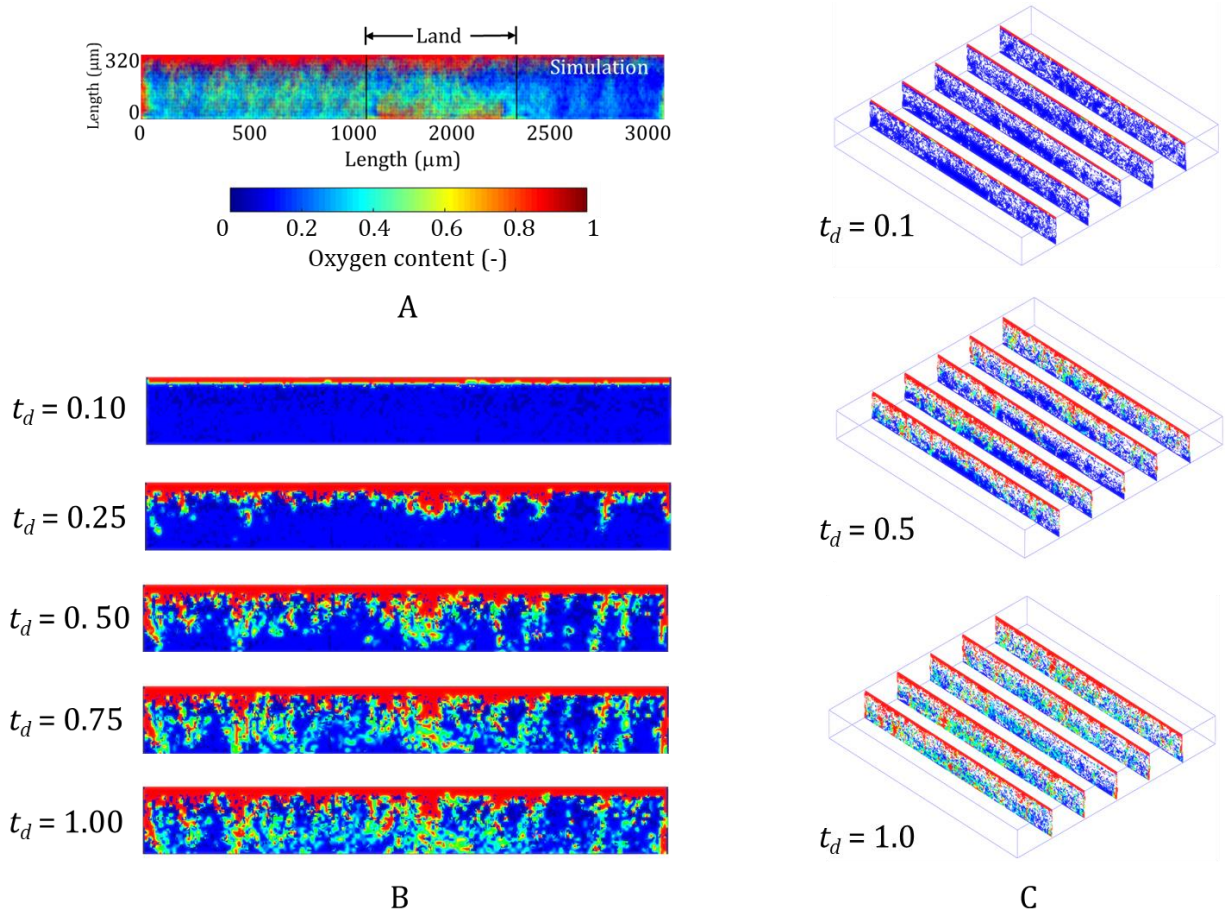

A

B

C

Figure S16. **CFD simulation with the uniform flux of oxygen on the top of PTL at 1 A/cm² with the flow rate of 2 mlpm.**

The aerophilic of oxygen was defined between the surface of oxygen-water with the contact angle of 10 degree. (A) 2D simulation of oxygen content in PTL at x-y plane by using Z-project method at steady state. (B) Cross section view on the middle of the sample that shows the time dependent simulation of oxygen transport in the PTL. (C) Isometric view with cross sections that shows the oxygen distribution in the PTL sample. Related to Figure 6.
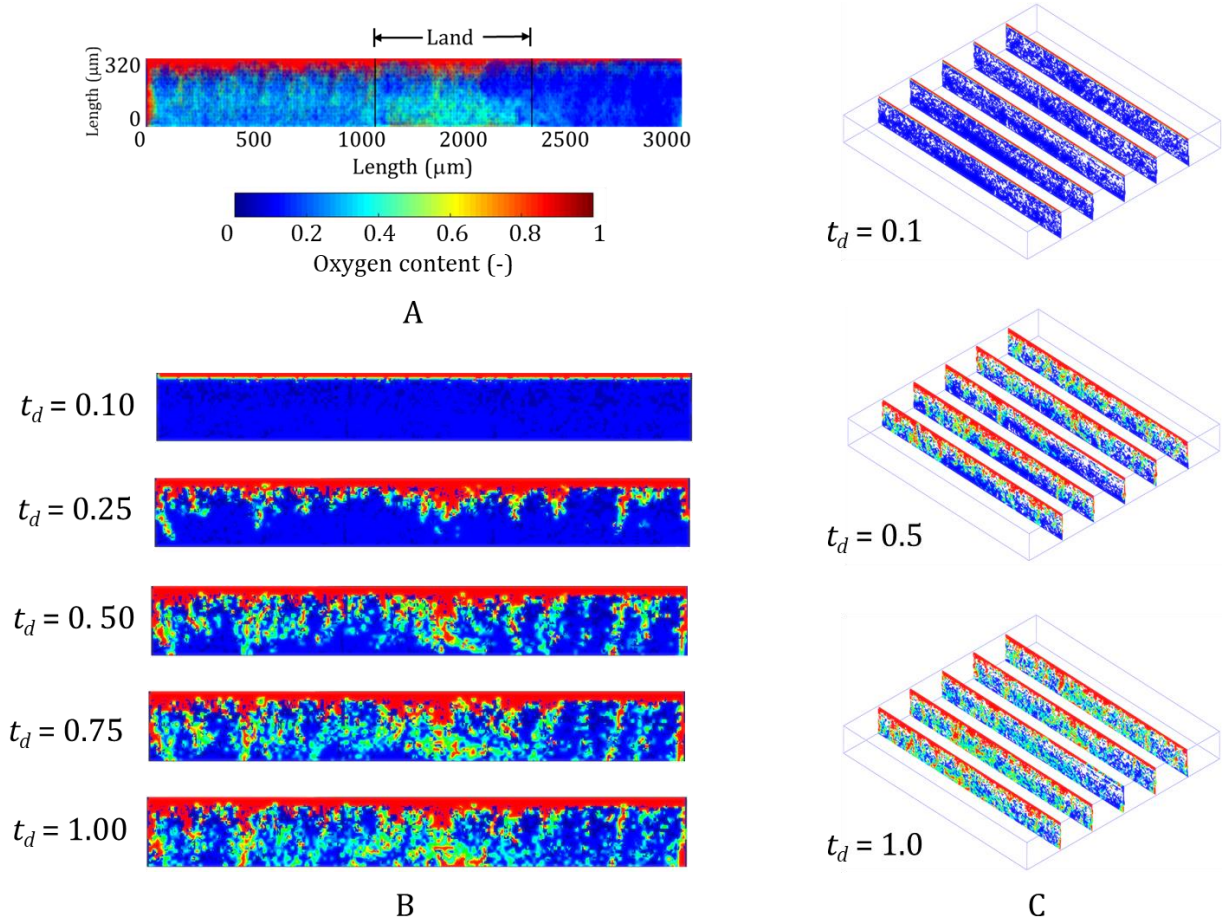
Figure S17. CFD simulation with the uniform flux of oxygen on the top of PTL at 4 A/cm^2 with the flow rate of 2 mlpm.

The aerophilic of oxygen was defined between the surface of oxygen-water with the contact angle of 10 degree. (A) 2D simulation of oxygen content in PTL at x-y plane by using Z-project method at steady state. (B) Cross section view on the middle of the sample that shows the time dependent simulation of oxygen transport in the PTL. (C) Isometric view with cross sections that shows the oxygen distribution in the PTL sample. Related to Figure 6.
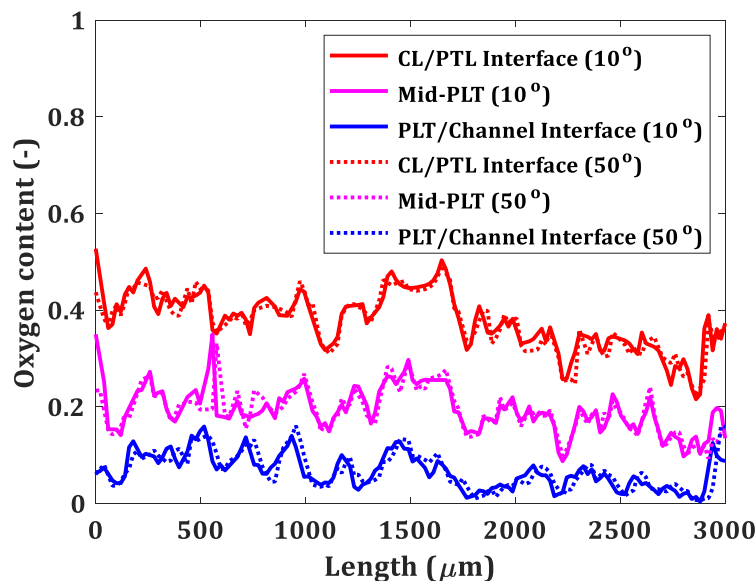
Figure S18. **The effect of wettability on oxygen content comparison between 10 and 50 degree of PTL contact angle.** Related to Figure 6.

REFERENCES

Alrwashdeh, S.S., Manke, I., Markötter, H., Klages, M., Göbel, M., Haußmann, J., Scholta, J., and Banhart, J. (2017). In Operando Quantification of Three-Dimensional Water Distribution in Nanoporous Carbon-Based Layers in Polymer Electrolyte Membrane Fuel Cells. ACS Nano 11, 5944–5949.

Chen, S., and Doolen, G.D. (1998). Lattice Boltzmann method for fluidflows. Annu. Rev. Fluid Mech. 30, 329–364.

Cooper, S.J., Bertei, A., Shearing, P.R., Kilner, J.A. and Brandon, N.P. (2016). TauFactor: An open-source application for calculating tortuosity factors from tomographic data. SoftwareX 5, 203–210.

De Carlo, F., Gürsoy, D., Marone, F., Rivers, M., Parkinson, D.Y., Khan, F., Schwarz, N., Vine, D.J., Vogt, S., Gleber, S.C., Narayanan, S., Newville, M., Lanzirotti, T., Sun, Y., Hong, Y.P., and Jacobsen, C. (2014). Scientific data exchange: A schema for HDF5-based storage of raw and analyzed data. J. Synchrotron Radiat. 21, 1224–1230.

d'Humieres, D. (2002). Multiple relaxation time Lattice Boltzmannmodels in three dimensions. Phil. Trans. R. Soc. Lond. A. 360, 437–451.

Doube, M., Klosowski, M.M., Arganda-Carreras, I., Cordelières, F.P., Dougherty, R.P., Jackson, J.S., Schmid, B., Hutchinson, J.R., and Shefelbine, S.J. (2010). BoneJ: Free and extensible bone

image analysis in ImageJ. Bone 47, 1076–1079.

Dowd, B.A., Campbell, G.H., Marr, R.B., Nagarkar, V. V., Tipnis, S. V., Axe, L., and Siddons, D.P. (1999). Developments in synchrotron x-ray computed microtomography at the National Synchrotron Light Source. Dev. X-Ray Tomogr. II 3772, 224–236.

Frisch, U., Hasslacher, B., and Pomeau, Y. (1986). Lattice-gas automata for the Navier–Stokes equation. Phys. Rev. Lett. 56, 1505–1508.

Holman, D.M., Brionnaud, R., and Abiza, Z. (2012). Solution to industrybenchmark problems with the Lattice-Boltzmann code XFlow.In: Proceeding in the European Congress on ComputationalMethods in Applied Sciences and Engineering (ECCOMAS),Vienna, Austria.

Kadyk, T., Bruce, D., and Eikerling, M. (2016). How to Enhance Gas Removal from Porous Electrodes. Scientific Reports. 6, 38780.

Leonard, E., Shum, A.D., Danilovic, N., Capuano, C., Ayers, K.E., Pant, L.M., Weber, A.Z., Xiao, X., Parkinson, D.Y., and Zenyuk, I. V. (2020). Interfacial analysis of a PEM electrolyzer using X-ray computed tomography. Sustain. Energy Fuels 4, 921–931.

Leonard, E., Shum, A.D., Normile, S., Sabarirajan, D.C., Yared, D.G., Xiao, X., and Zenyuk, I. V. (2018). Operando X-ray tomography and sub-second radiography for characterizing transport in polymer electrolyte membrane electrolyzer. Electrochim. Acta 276, 424–433.

McNamara, G.R., and Zanetti, G. (1988). Use of the Boltzmann equation to simulate lattice-gas automata. Phys. Rev. Lett. 61, 2332–2335.

Pelt, D.M., Gürsoy, D., Palenstijn, W.J., Sijbers, J., De Carlo, F., and Batenburg, K.J. (2016). Integration of TomoPy and the ASTRA toolbox for advanced processing and reconstruction of tomographic synchrotron data. J. Synchrotron Radiat. 23, 842–849.

Premnath, K., and Banerjee, S. (2012). On the three-dimensionalcentral moment Lattice Boltzmann method. J. Stat. Phys. 143, 747–761.

Satjaritanun, P., Hirano, S., Shum, A.D., Zenyuk, I. V., Weber, A.Z., Weidner, J.W., and Shimpalee, S. (2018). Fundamental Understanding of Water Movement in Gas Diffusion Layer under Different Arrangements Using Combination of Direct Modeling and Experimental Visualization. J. Electrochem. Soc. 165, F1115–F1126.

Satjaritanun, P., Hirano, S., Zenyuk, I. V., Weidner, J.W., Tippayawong, N., and Shimpalee, S. (2020). Numerical Study of Electrochemical Kinetics and Mass Transport inside Nano-Structural Catalyst Layer of PEMFC Using Lattice Boltzmann Agglomeration Method. J. Electrochem. Soc. 167, 013516. https://doi.org/10.1149/2.0162001jes

Satjaritanun, P., Weidner, J.W., Hirano, S., Lu, Z., Khunatorn, Y., Ogawa, S., Litster, S.E., Shum, A.D., Zenyuk, I. V., Shimpalee, S., 2017. Micro-Scale Analysis of Liquid Water Breakthrough inside Gas Diffusion Layer for PEMFC Using X-ray Computed Tomography and Lattice Boltzmann Method. J. Electrochem. Soc. 164, E3359–E3371.

Schneider, C.A., Rasband, and W.S., Eliceiri, K.W. (2012). NIH Image to ImageJ: 25 years of image analysis. Nat. Methods 9, 671–675.

Serov, A., Shum, A.D., Xiao, X., De Andrade, V., Artyushkova, K., Zenyuk, I. V. and Atanassov, P. (2018). Nano-structured platinum group metal-free catalysts and their integration in fuel cell electrode architectures. Appl. Catal. B Environ. 237, 1139–1147.

Shan, X., and Chen, H. (2007). A general multiple-relaxation-time Boltzmann collision model. Int. J. Mod. Phys. C. 18, 635–643.

Shrestha, P., Lee, C., Fahy, K.F., Balakrishnan, M., Ge, N., and Bazylak, A. (2020). Formation of Liquid Water Pathways in PEM Fuel Cells: A 3-D Pore-Scale Perspective. J. Electrochem. Soc. 167, 054516.

Shum, A.D., Parkinson, D.Y., Xiao, X., Weber, A.Z., Burheim, O.S. and Zenyuk, I. V. (2017). Investigating Phase-Change-Induced Flow in Gas Diffusion Layers in Fuel Cells with X-ray Computed Tomography. Electrochim. Acta 256, 279–290.

Witten, I.H., Frank, E., and Hall, M. (2011). Data Mining: Practical Machine Learning Tools and Techniques (Google eBook), Complementary literature None.

Zenyuk, I. V., Lamibrac, A., Eller, J., Parkinson, D.Y., Marone, F., Büchi, F.N., and Weber, A.Z. (2016). Investigating Evaporation in Gas Diffusion Layers for Fuel Cells with X-ray Computed Tomography. J. Phys. Chem. C 120, 28701–28711.

Zenyuk, I. V., Parkinson, D.Y., Hwang, G., and Weber, A.Z. (2015). Probing water distribution in compressed fuel-cell gas-diffusion layers using X-ray computed tomography. Electrochem. commun. 53, 24–28.